Running title: Microglial responses after irradiation

Microglia Adopt Temporally Specific Subtypes after Irradiation, Correlating with Neuronal Asynchrony

Alejandro Lastra Romero[1,14], Efthalia Preka[1,14], Giusy Pizzirusso[1,2,15], Luis Enrique Arroyo-García[2], [1,2,15], Georgios Alkis Zisiadis[1,15], Nuria Oliva-Vilarnau[3], Thea Seitz[1], Kai Zhou[1], Arturo Gonzalez Isla[2], Lara Friess[4], Ying Sun[5] , Alia Shamikh[6], Yiran Xu[7], Changlian Zhu[1,7,8], Carlos F. D. Rodrigues[1], André Fisahn[1], Bertrand Joseph[4], Lena-Maria Carlson[1,9], Adamantia Fragkopoulou[1], Volker M Lauschke[3,10,11,12] Christer Betsholtz[5,13], Ahmed M Osman[1,16*], Klas Blomgren[1,9,16,17*]

1. Department of Women's and Children's Health, Karolinska Institutet, 171 65 Stockholm, Sweden.
2. Department of Neurobiology, Care Sciences and Society, Division of Neurogeriatrics, Karolinska Institutet, 171 64, Solna, Sweden.
3. Department of Physiology and Pharmacology, Karolinska Institutet, 171 77 Stockholm, Sweden.
4. Institute of Environmental Medicine, Toxicology Unit, Karolinska Institutet, 171 77 Stockholm, Sweden.
5. Department of Immunology, Genetics and Pathology, Rudbeck Laboratory, Uppsala University.
6. Department of Clinical Pathology and Cytology, Karolinska University Hospital, 171 64 Stockholm, Sweden.
7. Henan Key Laboratory of Child Brain Injury, Institute of Neuroscience and Third Affiliated Hospital of Zhengzhou University, Zhengzhou, 450052, China.
8. Center for Brain Repair and Rehabilitation, Institute of Neuroscience and Physiology, University of Gothenburg, 405 30 Gothenburg, Sweden.
9. Pediatric Oncology, Karolinska University Hospital, 171 64 Stockholm, Sweden.
10. Center for Molecular Medicine, CMM, Karolinska Institutet and University Hospital, Visionsgatan 18, 171 64 Stockholm, Sweden.
11. Dr Margarete Fischer-Bosch Institute of Clinical Pharmacology, Stuttgart, Germany
12. University of Tübingen, Tübingen, Germany.
13. Integrated Cardio-Metabolic Centre, Department of Medicine, Karolinska Institutet, Novum, 141 57 Stockholm, Sweden.
14. Shared first authors
15. Equal contribution
16. Shared senior authors
17. Lead contact

* **Correspondence address:**
Ahmed M Osman, BVM, MVSc, PhD (Email: ahmed.osman@ki.se)

Klas Blomgren, MD, PhD (E-mail: klas.blomgren@ki.se)
Karolinska Institutet, Department of Women's and Children's Health,
Biomedicum Solnavägen 9, quarter A04
171 65 Stockholm, Sweden
Tel: +46 8-123 747 57

Summary

Cranial radiotherapy causes progressive neurocognitive impairments in cancer survivors. Neuroinflammation is believed to be a key contributor, but its dynamics and consequences for brain function remain poorly understood. Here, we performed comprehensive longitudinal profiling, from 6 hours to 1 year after irradiation (IR) of the mouse hippocampus, using transcriptomic, protein and histological analyses. We identified a delayed microglial response coupling interferon signaling to mitotic progression, and a subsequent induction of temporally regulated subtypes. IR rewired the parenchymal phagocyte profiles due to progressive microglial loss, failure of repopulation through self-renewal and compensatory generation of microglia-like cells derived from peripheral monocytes. These findings were confirmed in autopsied human brain. Finally, we demonstrate two phases of neuronal asynchrony, an early one associated with inflammation and a late one associated with synaptic aberrant regulation. These results provide comprehensive, longitudinal insights into microglia responses that can aid tailoring therapies to preserve cognition in cancer survivors.

Key words:

Radiotherapy, neuroinflammation, cognition, sequencing, hippocampus, cGAS-STING

Introduction

Cranial irradiation (IR) is standard of care in the treatment of high-grade primary and metastatic brain tumors. However, it causes long-term neurocognitive complications in 50-90% of the patients, especially children [1,2]. Impaired cognitive domains include learning, processing speed, memory, executive function and attention [3]. Attempts to omit upfront craniospinal IR in brain cancers with good prognosis aiming to reduce IR-associated neurotoxicity, by replacing it with focal IR, have failed [4]. IR-induced cognitive deficits are, thus, an unavoidable, debilitating clinical problem that demands careful attention, particularly since the overall survival rates and remaining life expectancies of children with brain tumors by far exceed those of adults, and are expected to improve even further with current advances in cancer therapies [5].

The molecular underpinnings of IR-induced cognitive deficits remain largely unknown. For the past two decades, a dominant hypothesis was depletion of postnatal hippocampal neurogenesis, a process by which of new neurons are continuously generated from dividing neural stem and progenitor cells (NSPCs) in the subgranular zone (SGZ), and important for maintaining learning and memory throughout life [6-9]. IR-induced depletion of neurogenesis has been linked to an increase in the number and activation status of microglia within the neurogenic zone, creating a hostile microenvironment that hinders NSPC proliferation and neuronal differentiation [10,11]. Despite the compelling evidence linking reduced neurogenesis to neuroinflammation [12], the negative effects of inflammation on brain functions and its consequent cognitive deficits are unlikely be limited to depletion of hippocampal neurogenesis, as evident from other CNS disease models [13].

Microglia, the resident immune cells and phagocytes in the brain, play key roles in neuroinflammation [14]. Microglia respond rapidly to IR and undergo series of molecular events, resulting in production of cytokines and chemokines and engulfment of dying NSPCs [15-17]. There is, as of yet, a fundamental lack of defined mechanisms by which the IR-induced microglial responses contribute to cognitive deficits. Current knowledge is based on studies performed in *in vitro* systems or *in vivo* based on one or few time points close to the time of IR, using conventional histological analyses and measurements of pre-selected inflammatory mediators in the brain [18]. Currently available data based on bulk or single cell transcriptomic analyses of post-IR microglial responses are limited to time points within days to weeks post-IR [16,19-21], resulting in a lack of high-resolution information about the delayed molecular events in microglia. Given the dynamic nature of microglia [22,23], and that post-IR cognitive deficits are delayed and progress over 5-10 years [1], it is imperative to investigate trajectories at the cellular and tissue level over a relevant period of time.

We performed unbiased, longitudinal *in vivo* studies of the post-IR inflammatory response in the hippocampus, a brain structure central to cognition [24], spanning both acute and chronic phases (6 hours to 1 year), using transcriptomics combined with histological and protein analyses. We uncovered delayed microglial 'reactivation' and induction of unique temporal subtypes yielding multifaceted inflammatory profiles.

Results

IR causes biphasic inflammatory waves in the hippocampus

We have previously shown that hippocampal microglia in the juvenile brain are activated as early as 2 h post-IR and return to baseline within 1 week (wk) [16]. Data from adult rodent models, however, suggest that IR induces persistent microglial activation and chronic neuroinflammation [12,25,26]. Thus, we asked whether long-term inflammation occurs also in the juvenile brain and, if so, what role(s) microglia play. To this end, we first performed a longitudinal unbiased bulk RNA sequencing (RNA-seq) analysis of hippocampal tissue from 6 h to 6 wk post-IR. Juvenile mice were subjected to whole-brain irradiation (WBI) with a single dose of 8 Gy. This IR dose is equivalent to a total radiation dose of 18 Gy, when delivered in repeated 2-Gy fractions, as in a clinical setting, estimated using the linear-quadratic (LQ) model and an α/β ratio of three for late effects in normal brain tissue [27].

Hippocampi were dissected 6 h (acute phase), 1 day (acute phase), 1 wk (early sub-acute phase), 2 wk (delayed sub-acute phase) and 6 wk (sub-chronic phase) post-IR, and from age-matched sham controls (SH) (Figure 1A). At all time points, principal component analysis (PCA) showed that IR samples were distinctly clustered separate from their respective SH samples (Figure 1B), indicating long-term transcriptomic alterations in the hippocampus post-IR. Numerous differentially expressed genes (DEGs; $q < 0.05$) between the SH and IR animals were detected as early as 6 h post-IR (Figure 1C). Downregulated DEGs peaked 1day post-IR and then decreased over time (Figure 1C; Supplementary list 1). The dynamics of upregulated DEGs were different. The number of upregulated DEGs peaked 6 h post-IR, decreased by 1 day and 1 wk, followed by a second increase at 2 wk, and a decrease again 6

wk post-IR (Figure 1C; Supplementary list 1), suggesting a second delayed response 2 wk post-IR. While the earlier alterations have been extensively studied [11,15-17,28], we focused our attention on this later response 2 wk post-IR.

Gene set enrichment analysis (GSEA) revealed activation ($p < 0.05$) of pathways associated with inflammation and response to viruses (Supplementary figure 1A). Out of the 58 upregulated DEGs, 27 genes were related to inflammation, the majority of which were involved in interferon (IFN) signaling pathways (Supplementary figures 1B and 1C), indicative of a second inflammatory wave mediated by IFN signaling. Targeted expression analysis of genes related the cytokines and chemokines revealed that chemokines were the most upregulated inflammatory mediators (Supplementary figure 1D). We found a significant induction of a set of chemokines within the first 24 h post-IR. At 1 wk, *Ccl12* was the only chemokine that remained significantly increased. At 2 wk, however, we detected a significant increase in the expression of *Cxcl10*, *Ccl5* (both belonging to interferon signaling pathways), *Ccl2* and *Ccl12*. The increased expression of *Ccl2* and *Ccl12* remained significant till 6 wk (Supplementary figure 1D). The biphasic inflammatory response was validated in independent hippocampal tissue at both RNA and protein level (Figures 1D-1I; Supplementary figure 1E). These data indicate that WBI causes a biphasic inflammatory response in the hippocampus, where a first wave occurs acutely, within the first 24 h post-IR, and a second, delayed wave occurs in the subacute phase, dominated by IFN signaling pathways.

Delayed microglial responses occurring post-IR

We next asked whether the second inflammatory wave detected 2 wk post-IR is driven by a second episode of microglial re-activation. Hippocampal microglia were selectively isolated,

based on CX3CR1 expression, at 2 and 6 wk post-IR, and processed for bulk RNA-seq [16] (Figure 2A). Samples from SH and IR microglia formed a clearly distinct clusters at both time points (Figure 2B), indicative of a delayed IR-induced response in microglia. In total, 415 and 1070 genes were differentially expressed at 2 and 6 wk, respectively (Figure 2C; Supplementary list 2), of which only 47 genes were overlapping between the two time points (Figure 2C). GSEA further revealed that microglia from both time points had distinct molecular profiles. At 2 wk, enriched pathways ($q < 0.05$) were related to P53 signaling, cell cycle progression, and response to viral infection (IFN signaling) (Figure 2D); while at 6 wk, enriched pathways were related to cell death (autophagy and necroptosis), innate immune response (TNF signaling, NOD-like receptor signaling, antigen processing and presentation), and response to viral infection (Figure 2E). Targeted analysis of genes related to cytokines and chemokines revealed an increased expression of *Cxcl10* at 2 wk, and *Tnf*, *Il6* and *Cxcl2* at 6 wk (Supplementary figure 2A).

To validate these temporal transcriptomic events, we first analyzed the microglial proliferative response post-IR. Proliferating cells ($Ki67^+$) were quantified in two distinct hippocampal regions, the molecular layer (ML) and the *cornu ammonis* 1 (CA1) region with the intention to not include the granule cell layer and SGZ, where NSPCs and their progenies often proliferate and microglia actively eliminate apoptotic cells [29]. The following time points post-IR were covered: 6 h (when the first wave of the inflammation occurred), 1 wk (when the first inflammatory wave was resolved), 2 wk and 6 wk (during and after the second inflammatory wave). $Ki67^+$ cells in the in these regions were either oligodendrocyte progenitors ($Olig2^+$ cells) or microglia ($Iba1^+$ cells) (Supplementary figure 2B). While the total number of $Ki67^+$ cells decreased 6 h and 6 wk post-IR (Supplementary figure 2C), phenotyping of $Ki67^+$ cells revealed that IR caused a striking shift in the identity of cycling

cells in the hippocampus. In the intact hippocampus (SH), Olig2$^+$ cells were the most abundant cycling cells (Olig2$^+$/Ki67$^+$), whereas post-IR, cycling cells were predominately Iba1$^+$ cells in both examined areas at 2 and 6 wk (Supplementary figures 2D - 2E). The number of proliferating microglia (Iba1$^+$/Ki67$^+$ cells) was significantly increased 2 wk post-IR (Figure 2F), while the number of Olig2$^+$/Ki67$^+$ cells decreased over time post-IR (Supplementary figure 2F). Finally, we validated the induction of *Tnf*, *Il6* and *Cxcl2* 6 wk post-IR in the hippocampus tissue using qPCR (Figure 2G; Supplementary figure 2G). Collectively, these results indicate that microglia undergo a delayed and temporally distinct re-activation post-IR, featured by upregulation of genes involved in IFN signaling, coupled with a wave of proliferation at 2 wk, and adoption of a neurotoxic phenotype at 6 wk.

Multiple microglial subtypes orchestrate the delayed response to IR

Next, we asked whether the observed delayed inflammatory response is exclusively driven by microglia or if also other cell types are involved. To gain better cellular and molecular resolutions, we dissected the hippocampi of IR mice and age-matched SH controls 2 wk post-IR. We developed a cell isolation protocol consisting of a rapid enzymatic digestion and a two-step myelin removal, using Percoll® gradients to obtain a viable single-cell suspension suitable for single-cell RNA sequencing (scRNA-seq) using the droplet-based method (10× Genomics Chromium) (Figure 3A). Clustering analysis revealed that our cell isolation protocol captured microglia and macrophages, glial cells (both astrocytes and oligodendrocytes), neurons, vascular cells (endothelial cells, pericytes, fibroblasts and myfibroblasts), and ependymal cells, from both SH and IR animals (Supplementary figures 3A and 3B). Microglia and neurons were the cell types with the most DEGs; however, the increased expression of inflammatory mediators observed in the hippocampal tissue at 2 wk (*e.g. Cxcl10* and *Ccl12*) were found in microglia (Supplementary figures 3C and 3D). Thus,

we focused our attention on analyzing the microglial cells in depth. Microglia from SH and IR were distinctly clustered (Figure 3B). Sub-clustering revealed 12 clusters (subpopulations), of which clusters 1, 3, 4, 6, 7, 9 and 10 were induced post-IR, referred to as radiation-associated microglia (RAM) henceforth (Figure 3C).

Next, we wanted to identify which microglial populations were responsible for the IFN response observed in bulk RNA-seq data, and those progressing into cell cycle. GSEA of signature genes of the RAM clusters revealed activation of pathways related to response to viruses (*i.e.* IFN signaling) in cluster 6, and cell cycle progression in clusters 7, 9 and 10, of which cluster 9 was also enriched in genes related to apoptosis (Figure 3D; Supplementary figure 3E). Representation of activated and suppressed pathways of all RAM clusters, as revealed by GSEA, are shown in (Supplementary figure 4A). These data indicate that RAM are heterogenous and mediate the second inflammatory wave observed 2 wk post-IR.

We next investigated which RAM subpopulation(s), drive these events. RNA velocity, an algorithm predicting future states of individual cell for the coming hours based on the ratio between spliced and non-spliced RNA [30,31], revealed that the microglial population with enriched IFN signaling (cluster 6) contained the driver cells of the events seen at this time point, including the mitotic progression (cluster 7, 9 and 10) (Figure 3E). We next looked closer at the microglial population 6 wk post-IR, as they appeared distinctly different from the 2-wk microglia in our bulk RNA-seq data. We applied a similar scRNA-seq approach, and sub-clustering revealed 14 clusters, of which clusters 2, 3, 4, 5, 7, 9, 10, 11 and 12 were RAM (Figure 3F and 3G). Again, GSEA of RAM clusters revealed activation of pathways related to IFN signaling and inflammatory responses, cell cycle, cell death, oxidative phosphorylation and leukocyte trans-endothelial migration (TEM) (Figure 3H).

Representations of activated and suppressed pathways in all RAM clusters, as revealed by GSEA, are shown in (Supplementary figure 5A).

RNA velocity analysis at this time point revealed RAM trajectories towards cluster 5, which was enriched in pathways related to cellular senescence, apoptosis, IFN and TNF signaling (Figure 3I). Finally, expression of *Tnf* and *Il6*, the two genes that increased post-IR in our bulk data at this time points, was found in cells belonging to multiple RAM clusters (Supplementary figures 6A and 6B). Together, these results show that specific signaling programs orchestrate induction of multiple microglial subtypes in the delayed post-IR inflammatory response.

IR activates the cytosolic DNA sensing system

Both genomic instability and mitotic progression with damaged DNA have been shown to result in nucleic acid leakage to the cytosol, generation of micronuclei, and activation of the cyclic GMP-AMP synthase (cGAS) and stimulator of interferon genes (STING) pathway that trigger type-I IFN signaling [32-34]. We hypothesized that the cGAS-STING pathway may regulate the observed IFN response in microglia due to IR-induced DNA damage and/or mitotic progression with damaged DNA. Cell cycle analysis of proliferating microglial populations observed in our scRNA-seq data at 2 wk revealed that cells were at different cell cycle stages (Figure 4A). Cells in cluster 7 were in S-phase and cells in cluster 9 and 10 had progressed to G2/M phase (expressing the M phase gene *Cdk1*), while upregulating *Cdkn1a*, DNA damage response gene, and subsets of these cells, especially in cluster 10, were expressing the IFN signaling related gene *Cxcl10* (Figure 4B).

Next, we experimentally tested whether the post-IR IFN response involved the cGAS-STING pathway. To this end, we irradiated the BV2 microglial cell line with a single dose of 8 Gy.

The IR response was confirmed by expression of the DNA damage response marker γH2AX 1 h post-IR (Supplementary figure 7A). IR resulted in increased expression of the IFN-related genes *Ifit1*, *Ifit3* and *Cxcl10*, as well as increased secretion of CXCL10 (Figures 4C-E), validating the IFN response in microglia post-IR. Using immunofluorescence, we found that IR significantly increased the fraction of cells with micronuclei, cGAS immunoreactivity and phosphorylated STING (pSTING) (Figures 4F and 4G). Immunoblotting further revealed increased levels of phosphorylated tank-binding kinase 1 (pTBK1), a canonical downstream component of this pathway (Figure 4H). Overall, these results suggest that IR activates the cytosolic DNA sensing system in microglia, and this may contribute to the observed IFN response post-IR.

Monocyte-derived macrophages engraft in the hippocampus and differentiate into microglia-like cells to compensate for the IR-induced loss of microglia.

Given the dramatic transcriptional profile changes in the hippocampal tissue and the microglial cells over time post-IR, we set out to explore a more chronic phase. Hippocampi were collected 6 months (mo) post-IR, and RNA from the whole tissue was processed for bulk RNA-seq (Figure 5A). We found 30 DEGs between SH and IR groups (p adjusted $<$ 0.01), of which 19 were up- and 11 downregulated, respectively. Most downregulated genes were related to microglia, whereas monocyte-derived macrophages (MDMs) signatures were upregulated (Figure 5B). To increase resolution, we performed scRNA-seq on sorted $CX3CR1^{+}$ cells [16]. Clustering analysis revealed 11 clusters, where cluster 1 stood out as distinctly separate from both SH and IR microglia (Figure 5C). Cells in this cluster were either lacking or had low expression of microglial signature genes such as *Sall1* and *Tmem119*, but expressed MDM-related genes, such as *Ms4a7* (Figure 5D; Supplementary figure 8A). Notably, to avoid the bias that may occur from selectively sorting CX3CR1 cells,

we performed scRNA-seq also on unsorted cells, as for the 2 and 6 wk time points, and we confirmed the post-IR MDM recruitment (Supplementary figure 8B).

RNA velocity revealed that MDMs display trajectories towards parenchymal microglia, suggesting a potential MDM differentiation into a microglial lineage (Figure 5E; Supplementary figure 8C). To validate these results and obtain spatial information on the distribution of MDMs, we performed immunofluorescence staining for Iba1 (labeling both microglia and MDMs) and Tmem119 (marker for parenchymal microglia). We found three distinct populations of Iba1^{+} cells in IR animals, distributed throughout the hippocampus. One population with a higher expression of Tmem119 (Tmem119^{high}, representing microglia) and two other populations either negative or with lower Tmem119 expression (Tmem119^{negative} and Tmem119^{low}, respectively, representing MDMs). Iba1^{+} cells with Tmem119^{high} or Tmem119$^{negative/low}$ were morphologically distinct, whereas Tmem119$^{negative/ow}$ cells had thicker processes, less arborization and smaller area of occupancy (Figure 5F; Supplementary figure 8D). Combined, these data indicate engraftment of MDMs into the hippocampus long post-IR and that they appear to differentiate into microglia-like cells.

Next, we asked why MDMs infiltrate the hippocampus despite microglia proliferation at earlier time points post-IR. Longitudinal quantification of Iba1^{+} cells post-IR (6 h to 6 mo) demonstrated a progressive loss of Iba1^{+} cells over time, reaching nearly 50% by 6 wk, followed by a near restoration by 6 mo, reducing the loss to 15% (Figure 5G). This led us to hypothesize that IR microglia fail to repopulate through self-renewal, and hence MDMs infiltrate the hippocampus to compensate for the loss. To test this, labeled proliferating cells between day 10 to 14 post-IR using 5-bromo-2'-deoxyuridine (BrdU), a thymidine analog incorporated by cycling cells during the S-phase [35], as these days fall within the proliferative

wave shown above. Animals were sacrificed either 2 h after the last BrdU injection (*i.e.* 2 wk post-IR) to assess proliferation or 4 wk later (*i.e.* 6 wk post-IR) to assess survival of the newborn cells (Figure 5H). Newborn microglia (Tmem119^{+}/BrdU^{+} cells) were quantified in the ML and CA1. As expected, IR led to a significant increase in the number of Tmem119^{+}/BrdU^{+} cells compared to SH at both time points, however, the number of Tmem119^{+}/BrdU^{+} cells was reduced by nearly 70% between 2 and 6 wk post-IR (Figure 5I; Supplementary figure 8E), indicating that the microglia born during the re-activation (*i.e.* 2 wk post-IR) do not survive. Importantly, qPCR analysis of the inflammatory mediators that were increased at earlier time points, showed no difference between SH and IR 6 mo post-IR (Supplementary figure 8F). Taken together, these results indicate continuous elimination of parenchymal microglia post-IR, failed attempts to compensate their loss by self-renewal, and consequently repopulation of their empty territories by recruited MDMs that differentiate into microglia-like cells. The observed phenotypic rewiring of the hippocampal resident immune cells post-IR represents a spontaneous elimination of IR-induced neurotoxic microglial phenotypes, concurrent with apparent normalization of the inflammatory responses observed at earlier phases post-IR.

MDMs begin infiltrating the hippocampus early post-IR and acquire a microglial phenotype over time

We computationally investigated the kinetics of the MDM infiltration into the IR hippocampus, and their differentiation into microglia-like cells. Analysis of the macrophage populations captured in our scRNA-seq datasets from the 2 wk, 6 wk, and 6 mo (unsorted cells) identified 8 clusters, of which 3 were IR-induced MDMs (refer to as iMDMs), clusters: 1 (iMDM1), 2 (iMDM2), and 5 (iMDM3) that were detectable as early as 2 wk post-IR (Supplementary figure 9A). After subclustering of iMDMs, iMDM1 yielded two subclusters,

iMDM1a and iMDM1b (Figures 6A), whose relative abundance varied over time (Figure 6A; Supplementary figure 9B). Using immunofluorescence, we further validated a significant increase in Iba1^{+}/Tmem119^{negative} cells in hippocampal tissue by 6 wk post-IR (Supplementary figure 9C). Next, we performed cell fate mapping using the CellRank-Moscot interface, an algorithm predicting the cellular stage across the experimental timeline based on likelihood [36,37]. Unsupervised computation for initial states revealed that a subset of iMDM3 at 2 and 6 wk as initial iMDMs and subset of cells belonging to iMDM1 and iMDM2 at 6 mo as terminal state (Figure 6B; Supplementary figure 9D). To confirm these findings, we assessed the expression of the microglia signature gene *Tmem119* in iMDMs and we found minimal expression in iMDM3 (the initial state of iMDMs), intermediate iMDM1b, and higher in iMDM1a and iMDM2, suggesting that iMDM1 and iMDM2 were the cells differentiated into microglia-like cells (Figure 6C). Moreover, morphological analysis of the Iba1^{+}/Tmem119$^{negative\ and\ low}$ cells revealed increased arborization of these cells at 6 mo compared to 6 wk (Supplementary figure 9E), compatible with adoption of a more microglia-like morphology over the time.

We next performed an unsupervised analysis of chemokine receptor expression in iMDMs as a proxy to possible signaling axes for recruiting these cells to the hippocampus post-IR. We found that *Ccr2* was expressed by initial state cells (iMDM3), but not by iMDM1 and 2 (Figure 6D). iMDM3 displayed a minimal expression of the *Cx3cr1*, another microglia signature gene whose expression was higher in iMDM1 and iMDM2 (Figure 6D), further supporting iMDM3 being the initial state, and in line with a previous report [38] demonstrating a role of CCR2 in recruiting MDMs into the brain. We also found a subset of iMDM3 expressing *Ccr1*, *Ccr5*, *Cxcr3* and *Cxcr4* (Figure 6D). This suggests a role for these chemokine receptors in MDM recruitment, in addition to CCR2, as supported by significantly

increased Iba1^{+}/Tmem119^{negative} cells in *Ccr2* deficient mice 6 wk post-IR (Supplementary figure 9F). The expression of *Ccr1*, *Ccr5*, and *Cxcr4* remained in a subset of iMDM2 (differentiated into microglia-like cells) (Figure 6D).

We next wanted to investigate the source of iMDMs. Recent work has demonstrated both blood and CNS-associated bone marrow in the skull and vertebrae as reservoirs for CNS infiltrating myeloid cells under pathological conditions [39]. Thus, we compared the iMDMs from the 6 wk time point, containing both initial *Ccr2* expressing and differentiated cells, with the previously published scRNA-seq data of CNS-infiltrated MDMs recruited from blood or CNS-associated bone marrow [39]. We found that iMDMs overlapped with subsets in both populations, suggesting that both sources could serve as the origin of iMDMs (Supplementary figures 10A -10C).

Finally, analysis of cancer-free hippocampal tissue sections from an autopsied brain collected 5 years after craniospinal irradiation of a medulloblastoma patient, demonstrated two distinct microglial populations: IBA1^{+}/TMEM119^{high} and IBA1^{+}/TMEM119^{low}, that were not detected in hippocampal tissue obtained from an autopsied adult donor with no known history of a neurological condition, demonstrating that post-IR MDM-derived microglia-like cells occur also in humans (Figure 6E; Supplementary figures 11A and 11B). Collectively, our data indicate that MDMs infiltrate the hippocampus early post-IR and differentiate into microglial-like cells over the time.

The post-IR microglial alterations persist long-term, but without active inflammatory responses

We used scRNA-seq to explore the molecular profiles of microglia at a much later time point, one year (yr) post-IR (Figure 6F). SH and IR microglia overlapped to a greater extent compared with earlier time points, with some exceptions (Figure 6G). Subclustering revealed 13 clusters, of which clusters 6, 9 and 10 were enriched in SH animals, and cluster 6 was nearly absent in IR animals (Figure 6H). GSEA of cluster 6 revealed enrichment of pathways related to neurons and synapses (Supplementary figure 12A), while RAM clusters 5 and 7 were enriched in pathways related to oxidative phosphorylation, protein processing, synapses and lysosomes, and cluster 12 was enriched in MDM genes (Supplementary figures 12A and 12B). At this late time point the number of Iba1^{+} cells still significantly lower (~15%) post-IR (Figure 6I), and IR animals tended to have lower expression of genes encoding inflammatory mediators, significantly so for *Ifit1*, *Cxcl10* and *Il6* (Figure 6J; Supplementary figures 12C and 12D). Together, these data demonstrate that the post-IR microglial loss persists, and long-term alterations of microglia appear not related to production of inflammatory mediators, but rather to phagocytosis and synaptic regulation.

The long-term effects of IR on microglia are initiated at an early phase

To connect the temporal molecular events occurring in RAM over time, we integrated our previously published scRNA-seq datasets from microglia (CX3CR1^{+} cells) isolated 6 h and 1 wk post-IR [16] with the datasets generated in this study (*i.e.* 2 wk, 6 wk, 6 mo and 1 yr), both RAM and age-matched SH (Figures 7A and 7B). SH microglia clustered in an age-dependent manner (Figures 7A). Interestingly, the corresponding 2-wk SH microglia (= P39) clustered separately from both the SH microglia of the earlier time points (6 h and 1 wk), as well as the later time point (6 wk) (Figures 7A), likely because this time point falls within the middlescence stage [40], when the brain undergoes substantial structural and functional alterations, including synaptic plasticity [41]. For RAM, however, the developmental pattern

was perturbed. RAM from 6 h and 1 wk clustered separately from each other, but also distinctly separated from other RAM of later time points (Figure 7B). Importantly, subsets of the 2-wk, 6-wk, 6-mo and 1-yr RAM clustered together (Figure 7B), suggesting that the alterations of RAM were induced during early phases post-IR.

We reconstructed the molecular trajectories in SH microglia and RAM over time using the CellRank-Moscot tool and set the 6 h microglia as initial state as this was the earliest time point collected. In SH animals, the 1 yr time point was determined as the terminal state, whereas in RAM, the terminal states were scattered between 6 wk, 6 mo and 1 yr time points (Figure 7C). Moreover, in SH, intermediate trajectories between the 2 wk, 6 wk and 6 mo time points were observed, before committing to a terminal state (Figure 7C). In RAM, projections towards terminal states were either directly from the 6 h-RAM, or via the 2-wk RAM as an intermediate state (Figure 7D). Importantly, the 2-wk RAM enriched in genes related to IFN signaling and cell cycle were an intermediate state (Figure 7D; Supplementary figure 13A), suggesting that the uncovered, delayed IFN signaling, and mitotic progression are likely crucial for the long-term effects of IR on hippocampal function.

Hippocampal circuitry asynchrony occurs 6 wk and 1 yr post-IR

Lastly, we wanted to correlate the microglial rewiring and inflammatory dynamics to neuronal function. To this end, we evaluated hippocampal gamma oscillatory activity 2 wk, 6 wk, 6 mo and 1 yr post-IR (Figures 7E and 7F), allowing for evaluation of neuronal firing patterns and circuitry rhythmicity involved in cognitive behaviors [42,43]. We found that the power and rhythmicity (as judged by the frequency variance) in the gamma range were comparable between the IR and the SH animals 2 wk post-IR (Figures 7F-7I). At 6 wk, however, we detected a profound decrease in gamma oscillation power in IR hippocampi,

concurrent with an increase in the frequency variance (Figures 7F-7I). At 6 mo, the gamma oscillation power had partially recovered in IR hippocampi (Figures 7F-7I) and differences in rhythm regularity (*i.e.* frequency variance) were normalized at this time point (Figures 7F-7I). Interestingly, we found a subsequent robust decrease in the gamma oscillation power 1 yr post-IR, (Figures 7F-7I).

Discussion

Microglia shape the physio-anatomical neuronal properties through synaptic pruning and secretion of trophic factors to maintain proper neuronal function [14,44-46]. Perturbed microglial-neuronal interaction due to microglial hyperreactivity or dysfunction may cause neuronal dysfunction, reflected in impaired cognition, as documented in numerous CNS disease models [14] . Impaired cognition is a hallmark complication in CNS cancer survivors treated with cranial radiotherapy [1]. Microglia play pivotal roles in IR-induced neurotoxicity through secretion of inflammatory molecules, generation of reactive oxygen species and excessive synaptic elimination [18]. Despite this consensus in the field, there is no successful treatment targeting microglial responses to prevent or reverse the IR-induced cognitive deficits. Here, we uncover numerous hippocampal RAM subtypes induced during a time course from hours to one year post-IR. We show that RAM are highly heterogeneous and follow unique temporally-regulated molecular programs resulting in multifaceted inflammatory profiles.

IFN signaling has been implied in the development of cognitive deficits in various CNS disease models [47-49]. In our IR model, we observed biphasic inflammatory phases in the hippocampal tissue, an acute wave occurring within hours post-IR and a delayed wave after 2 wk, featured by IFN signaling coupled with microglial mitotic progression, followed by increased levels of genes encoding the neurotoxic cytokines TNFα and IL-6 6 wk post-IR, coinciding with neuronal network asynchrony, a combination of events often linked to

impaired cognitive performance in CNS disease models [50-52]. We previously showed that hippocampal circuits are compromised in mouse models of neurodegenerative diseases, where microglia play pivotal roles [42,53,54], and targeting neuroinflammation rescues the hippocampal gamma oscillatory activity and cognitive performance in these models [55]. The neuronal asynchrony was partially recovered at 6 mo, overlapping with spontaneous elimination of irradiated parenchymal microglia, repopulation with MDMs, and normalized levels of genes encoding TNFα and IL-6 in the hippocampal tissue. Indeed, elimination of microglia post-IR has been shown to yield improved cognitive performance in animal models when assessed shortly after repopulation [26,56], however, the duration of this improvement remains unknown, especially considering the subsequent neuronal asynchrony 1 year post-IR with no signs of increased expression of inflammatory mediators, rather the opposite. This argues against a chronic inflammation late post-IR, making it unlikely that the second neuronal asynchrony is linked to active inflammatory responses. Featured regulated pathways at this time point were related to phagocytosis and neuronal synapses and indicates synaptic dysregulation by microglia. Nevertheless, the delayed neuronal asynchrony may still be a secondary consequence of the initial inflammatory events post-IR, leading to engagement of other cell type(s) and mediating these late effects, as was previously shown in the context of chemotherapy-induced neurotoxicity [57]. Adverse effects of IR on the brain are not limited to microglia or inflammation, other consequences, such as impaired neurogenesis, demyelination, gliosis, vascular abnormalities, and direct damage to neurons, are expected to contribute [1].

Radiation causes DNA damage and genomic instability and cells that fail to repair their DNA may undergo cell death or cellular senescence [58,59]. Senescent cells often resist cell death, do not replicate, and secret soluble factors, known as senescence-associated secretory phenotype

(SASP), affecting the functions of neighboring cells [60]. Microglia express the DNA damage response and cell cycle arrest genes *Cdkn1a* and *Ccng1* early post-IR [16], but despite this, previous work [12] and this study demonstrated increased microglial proliferative activity. Mitotic progression with damaged DNA or chromosomal instability activates the cGAS-STING pathway, leading to induction of type-I IFN signaling [32,61], in turn resulting in cellular senescence in neighboring cells via production of SASP [62,63]. In this study, we uncovered subsets of microglia characterized by IFN signaling as well as mitotic progression with damaged DNA. Our *in vitro* experiments further showed that IR can activate the cytosolic DNA sensing system in microglia, as judged by increased expression of cGAS, pSTING and pTBK1. Thus, future studies targeting the components of cGAS-STING pathway to dampen the post-IR IFN response are warranted; especially since we detected elevated levels of *Tnf* and *Il6*, both classified as SASP factors [64] 6 wk post-IR, and that the observed IFN response 2 wk post-IR appears to drive the increased levels of these inflammatory mediators.

Our results demonstrated rewiring of hippocampal parenchymal phagocytes after IR. The recruitment of MDMs into the brain post-IR has been reported earlier; using histological and bulk RNA-seq MDMs were shown to infiltrate the brain post-IR and differentiate into microglia-like cells [65-68]. Here we provide single-cell resolution and longitudinal characterization of the kinetics and the molecular phenotypic transition into microglial-like cells. Our results not only confirm the role of CCR2 as a key chemokine receptor for recruiting MDMs into the postnatal brain [38], but also suggests a role for other chemokine receptors, such as CCR1 and CCR5, in this process. The detection of MDMs in the hippocampus of *Ccr2*-deficient mice post-IR further supports this, and is consistent with what found in non-CNS tissue [69], and also explains the earlier finding that increased *Ccr1* expression post-IR remained significantly higher in *Ccr2*-deficient mice [70]. These chemokine

receptors may function in synergy to achieve efficient MDM recruitment into the hippocampus post-IR. Indeed, we observed elevations of CCL2 and CCL12, both of which are ligands for CCR1 and CCR2. While CCL2 followed the biphasic inflammatory pattern, CCL12 remained significantly elevated at the protein level for at least 6 wk post-IR, when the initially recruited cells (iMDM3) were abundant, suggesting a key role for CCL12 in MDM recruitment to the hippocampus post-IR. Comparison of the molecular profile of the post-IR MDMs with previously published datasets of blood- or CNS-associated bone marrow-derived MDMs [39] suggested that both sources could be the origin of MDMs. Previous work has demonstrated the blood-sourced MDM infiltration into the IR brain by systemic injection of bone marrow-derived cells [68]. To conclusively establish the CNS-associated bone marrow as a reservoir of MDMs post-IR, a cell tracing approach would be necessary.

We provide a single-cell level characterization of microglial responses from 6 h to 1 y after brain IR. The data serve as a resource for defining novel biomarkers associated with brain IR, measured in cerebrospinal fluid or blood. The uncovered re-activation of microglia 2 w post-IR, characterized by IFN signaling and proliferation despite DNA damage, offers potential pathways to counteract subsequent negative consequences on the hippocampal and other functions. However, given the anti-tumor properties mediated by IFN signaling [71], such approaches should be considered with caution. Finally, given that MDMs and parenchymal microglia display functional differences in animal models mimicking bacterial infection [65,66], it would be relevant to investigate how the rewired phagocytes would react to a secondary brain injury, such as re-irradiation or tumor relapse.

Acknowledgements

We express our deep gratitude to the patients and families that donated clinical samples, and the Swedish Children's Tumor Bank (Barntumörbanken) for providing the patient materials. This work was supported by the Swedish Childhood Cancer Fund, the Swedish Cancer Foundation, the Swedish Research Council, grants provided by the Stockholm County Council (ALF projects), Radiumhemmets Forskningsfonder, the Frimurare Barnhus Foundation in Stockholm, the KI Foundation for Research, the Märta and Gunnar V. Philipson Foundation, the Swedish Brain Foundation. AO gratefully acknowledges support from Stiftelsen Samariten, KI Foundation for Research, and Erik Rönnbergs Stipendium. VML was supported by the Swedish Research Council [grant numbers: 2021-02801 and 2023-03015] and the Robert Bosch Stiftung (Stuttgart, Germany). CB was supported by The Karolinska Institutet, Center for Innovative Medicine grant (CIMED).

The authors acknowledge support from the National Genomics Infrastructure in Stockholm funded by Science for Life Laboratory, the Knut and Alice Wallenberg Foundation and the Swedish Research Council, and SNIC/Uppsala Multidisciplinary Center for Advanced Computational Science for assistance with massively parallel sequencing, and access to the UPPMAX computational infrastructure.

We are grateful to Hajar Ba Omar and Jan-Bernd Stukenborg for sharing their expertise on immunofluorescence staining of the patient tissues. We would also like to thank the following core facilities at the Karolinska Institutet: the X-ray Core Facility, the Flow Cytometry Core Facility for assisting with the microglia sorting, the Bioinformatics and Expression Analysis (BEA) for bulk RNA-seq; the Eukaryotic Single Cell Genomics Facility (ESCG) for running the scRNA-seq.

Author contributions

A.M.O. and K.B. conceived and designed the study. A.L.R., E.P., A.M.O. A.Fr. and K.B. interpreted the results and wrote the manuscript. A.L.R., E.P., G.A.Z., K.Z., C.F.D.R. and A.M.O. performed the animal experiments. A.L.R., G.P., G.A.Z., T.S. and A.M.O., performed the histological analyses. A.L.R., E.P. and A.M.O. performed isolation of microglia and whole-brain cells for transcriptomic analyses. A.L.R, and T.S. performed the qPCR. K.Z. Y.X. and C.Z. contributed to bulk RNA-seq data. A.L.R., N.O-V. and V.M.L. analyzed the bulk RNA-seq data. E.P. performed single-cell RNA-seq and computational analyses. Y.S. and C.B. contributed to the single-cell RNA-seq analysis. L.E.A.G., G.P., A.G.I. and A.Fi. performed and analyzed the neuronal gamma oscillations. A.L.R., T.S., L.F., and B.J. contributed to BV2 experiments and immunoblotting experiments. L-M.C., A.S. and K.B. reviewed and annotated the clinical data. All authors discussed the results, commented on, or edited the manuscript.

Disclosure of Potential Conflicts of Interest

V.M.L. is co-founder and owner of HepaPredict AB. The other authors declare no competing of interests.

References

1. Makale, M.T., McDonald, C.R., Hattangadi-Gluth, J.A., and Kesari, S. (2017). Mechanisms of radiotherapy-associated cognitive disability in patients with brain tumours. Nat Rev Neurol *13*, 52-64. 10.1038/nrneurol.2016.185.
2. Palmer, J.D., Tsang, D.S., Tinkle, C.L., Olch, A.J., Kremer, L.C.M., Ronckers, C.M., Gibbs, I.C., and Constine, L.S. (2021). Late effects of radiation therapy in pediatric patients and survivorship. Pediatr Blood Cancer *68 Suppl 2*, e28349. 10.1002/pbc.28349.

3. Turnquist, C., Harris, B.T., and Harris, C.C. (2020). Radiation-induced brain injury: current concepts and therapeutic strategies targeting neuroinflammation. Neurooncol Adv *2*, vdaa057. 10.1093/noajnl/vdaa057.

4. Gupta, T., Pervez, S., Dasgupta, A., Chatterjee, A., Epari, S., Chinnaswamy, G., and Jalali, R. (2022). Omission of Upfront Craniospinal Irradiation in Patients with Low-Risk WNT-Pathway Medulloblastoma Is Associated with Unacceptably High Risk of Neuraxial Failure. Clin Cancer Res *28*, 4180-4185. 10.1158/1078-0432.CCR-22-0758.

5. Girardi, F., Allemani, C., and Coleman, M.P. (2019). Worldwide Trends in Survival From Common Childhood Brain Tumors: A Systematic Review. J Glob Oncol *5*, 1-25. 10.1200/JGO.19.00140.

6. Aimone, J.B., Li, Y., Lee, S.W., Clemenson, G.D., Deng, W., and Gage, F.H. (2014). Regulation and function of adult neurogenesis: from genes to cognition. Physiol Rev *94*, 991-1026. 10.1152/physrev.00004.2014.

7. Monje, M., and Dietrich, J. (2012). Cognitive side effects of cancer therapy demonstrate a functional role for adult neurogenesis. Behav Brain Res *227*, 376-379. 10.1016/j.bbr.2011.05.012.

8. Bostrom, M., Kalm, M., Karlsson, N., Hellstrom Erkenstam, N., and Blomgren, K. (2013). Irradiation to the young mouse brain caused long-term, progressive depletion of neurogenesis but did not disrupt the neurovascular niche. J Cereb Blood Flow Metab *33*, 935-943. 10.1038/jcbfm.2013.34.

9. Zanni, G., Goto, S., Fragopoulou, A.F., Gaudenzi, G., Naidoo, V., Di Martino, E., Levy, G., Dominguez, C.A., Dethlefsen, O., Cedazo-Minguez, A., et al. (2021). Lithium treatment reverses irradiation-induced changes in rodent neural progenitors and rescues cognition. Mol Psychiatry *26*, 322-340. 10.1038/s41380-019-0584-0.

10. Monje, M.L., Mizumatsu, S., Fike, J.R., and Palmer, T.D. (2002). Irradiation induces neural precursor-cell dysfunction. Nat Med *8*, 955-962. 10.1038/nm749.

11. Kalm, M., Fukuda, A., Fukuda, H., Ohrfelt, A., Lannering, B., Bjork-Eriksson, T., Blennow, K., Marky, I., and Blomgren, K. (2009). Transient inflammation in neurogenic regions after irradiation of the developing brain. Radiat Res *171*, 66-76. 10.1667/RR1269.1.

12. Monje, M.L., Toda, H., and Palmer, T.D. (2003). Inflammatory blockade restores adult hippocampal neurogenesis. Science *302*, 1760-1765. 10.1126/science.1088417.

13. DiSabato, D.J., Quan, N., and Godbout, J.P. (2016). Neuroinflammation: the devil is in the details. J Neurochem *139 Suppl 2*, 136-153. 10.1111/jnc.13607.

14. Colonna, M., and Butovsky, O. (2017). Microglia Function in the Central Nervous System During Health and Neurodegeneration. Annu Rev Immunol *35*, 441-468. 10.1146/annurev-immunol-051116-052358.

15. Kalm, M., Lannering, B., Bjork-Eriksson, T., and Blomgren, K. (2009). Irradiation-induced loss of microglia in the young brain. J Neuroimmunol *206*, 70-75. 10.1016/j.jneuroim.2008.11.002.

16. Osman, A.M., Sun, Y., Burns, T.C., He, L., Kee, N., Oliva-Vilarnau, N., Alevyzaki, A., Zhou, K., Louhivuori, L., Uhlen, P., et al. (2020). Radiation Triggers a Dynamic Sequence of Transient Microglial Alterations in Juvenile Brain. Cell Rep *31*, 107699. 10.1016/j.celrep.2020.107699.

17. Han, W., Umekawa, T., Zhou, K., Zhang, X.M., Ohshima, M., Dominguez, C.A., Harris, R.A., Zhu, C., and Blomgren, K. (2016). Cranial irradiation induces transient microglia accumulation, followed by long-lasting inflammation and loss of microglia. Oncotarget *7*, 82305-82323. 10.18632/oncotarget.12929.

18. Liu, Q., Huang, Y., Duan, M., Yang, Q., Ren, B., and Tang, F. (2022). Microglia as Therapeutic Target for Radiation-Induced Brain Injury. Int J Mol Sci *23*. 10.3390/ijms23158286.

19. Padilla, O., Minns, H.E., Wei, H.J., Fan, W., Webster-Carrion, A., Tazhibi, M., McQuillan, N.M., Zhang, X., Gallitto, M., Yeh, R., et al. (2024). Immune Response following FLASH and Conventional Radiation in Diffuse Midline Glioma. Int J Radiat Oncol Biol Phys. 10.1016/j.ijrobp.2024.01.219.

20. Voshart, D.C., Oshima, T., Jiang, Y., van der Linden, G.P., Ainslie, A.P., Reali Nazario, L., van Buuren-Broek, F., Scholma, A.C., van Weering, H.R.J., Brouwer, N., et al. (2024). Radiotherapy induces persistent innate immune reprogramming of microglia into a primed state. Cell Rep *43*, 113764. 10.1016/j.celrep.2024.113764.

21. Li, M.D., Burns, T.C., Kumar, S., Morgan, A.A., Sloan, S.A., and Palmer, T.D. (2015). Aging-like changes in the transcriptome of irradiated microglia. Glia *63*, 754-767. 10.1002/glia.22782.

22. Nimmerjahn, A., Kirchhoff, F., and Helmchen, F. (2005). Resting microglial cells are highly dynamic surveillants of brain parenchyma in vivo. Science *308*, 1314-1318. 10.1126/science.1110647.

23. Arcuri, C., Mecca, C., Bianchi, R., Giambanco, I., and Donato, R. (2017). The Pathophysiological Role of Microglia in Dynamic Surveillance, Phagocytosis and Structural Remodeling of the Developing CNS. Front Mol Neurosci *10*, 191. 10.3389/fnmol.2017.00191.

24. Bird, C.M., and Burgess, N. (2008). The hippocampus and memory: insights from spatial processing. Nat Rev Neurosci *9*, 182-194. 10.1038/nrn2335.

25. Moravan, M.J., Olschowka, J.A., Williams, J.P., and O'Banion, M.K. (2011). Cranial irradiation leads to acute and persistent neuroinflammation with delayed increases in

T-cell infiltration and CD11c expression in C57BL/6 mouse brain. Radiat Res *176*, 459-473. 10.1667/rr2587.1.

26. Acharya, M.M., Green, K.N., Allen, B.D., Najafi, A.R., Syage, A., Minasyan, H., Le, M.T., Kawashita, T., Giedzinski, E., Parihar, V.K., et al. (2016). Elimination of microglia improves cognitive function following cranial irradiation. Sci Rep *6*, 31545. 10.1038/srep31545.

27. Fowler, J.F. (1989). The linear-quadratic formula and progress in fractionated radiotherapy. Br J Radiol *62*, 679-694. 10.1259/0007-1285-62-740-679.

28. Blomstrand, M., Kalm, M., Grander, R., Bjork-Eriksson, T., and Blomgren, K. (2014). Different reactions to irradiation in the juvenile and adult hippocampus. Int J Radiat Biol *90*, 807-815. 10.3109/09553002.2014.942015.

29. Sierra, A., Encinas, J.M., Deudero, J.J., Chancey, J.H., Enikolopov, G., Overstreet-Wadiche, L.S., Tsirka, S.E., and Maletic-Savatic, M. (2010). Microglia shape adult hippocampal neurogenesis through apoptosis-coupled phagocytosis. Cell Stem Cell *7*, 483-495. 10.1016/j.stem.2010.08.014.

30. La Manno, G., Soldatov, R., Zeisel, A., Braun, E., Hochgerner, H., Petukhov, V., Lidschreiber, K., Kastriti, M.E., Lonnerberg, P., Furlan, A., et al. (2018). RNA velocity of single cells. Nature *560*, 494-498. 10.1038/s41586-018-0414-6.

31. Bergen, V., Lange, M., Peidli, S., Wolf, F.A., and Theis, F.J. (2020). Generalizing RNA velocity to transient cell states through dynamical modeling. Nature Biotechnology *38*, 1408-1414. 10.1038/s41587-020-0591-3.

32. Harding, S.M., Benci, J.L., Irianto, J., Discher, D.E., Minn, A.J., and Greenberg, R.A. (2017). Mitotic progression following DNA damage enables pattern recognition within micronuclei. Nature *548*, 466-470. 10.1038/nature23470.

33. Mackenzie, K.J., Carroll, P., Martin, C.A., Murina, O., Fluteau, A., Simpson, D.J., Olova, N., Sutcliffe, H., Rainger, J.K., Leitch, A., et al. (2017). cGAS surveillance of micronuclei links genome instability to innate immunity. Nature *548*, 461-465. 10.1038/nature23449.

34. Decout, A., Katz, J.D., Venkatraman, S., and Ablasser, A. (2021). The cGAS-STING pathway as a therapeutic target in inflammatory diseases. Nat Rev Immunol *21*, 548-569. 10.1038/s41577-021-00524-z.

35. Kuhn, H.G., and Cooper-Kuhn, C.M. (2007). Bromodeoxyuridine and the detection of neurogenesis. Curr Pharm Biotechnol *8*, 127-131. 10.2174/138920107780906531.

36. Lange, M., Bergen, V., Klein, M., Setty, M., Reuter, B., Bakhti, M., Lickert, H., Ansari, M., Schniering, J., Schiller, H.B., et al. (2022). CellRank for directed single-cell fate mapping. Nature Methods *19*, 159-170. 10.1038/s41592-021-01346-6.

37. Lange, M., Piran, Z., Klein, M., Spanjaard, B., Klein, D., Junker, J.P., Theis, F.J., and Nitzan, M. (2023). Mapping lineage-traced cells across time points with moslin. bioRxiv, 2023.2004.2014.536867. 10.1101/2023.04.14.536867.

38. Mildner, A., Schmidt, H., Nitsche, M., Merkler, D., Hanisch, U.K., Mack, M., Heikenwalder, M., Bruck, W., Priller, J., and Prinz, M. (2007). Microglia in the adult brain arise from Ly-6ChiCCR2+ monocytes only under defined host conditions. Nat Neurosci *10*, 1544-1553. 10.1038/nn2015.

39. Cugurra, A., Mamuladze, T., Rustenhoven, J., Dykstra, T., Beroshvili, G., Greenberg, Z.J., Baker, W., Papadopoulos, Z., Drieu, A., Blackburn, S., et al. (2021). Skull and vertebral bone marrow are myeloid cell reservoirs for the meninges and CNS parenchyma. Science *373*. 10.1126/science.abf7844.

40. Bian, W.J., Brewer, C.L., Kauer, J.A., and de Lecea, L. (2022). Adolescent sleep shapes social novelty preference in mice. Nat Neurosci *25*, 912-923. 10.1038/s41593-022-01076-8.

41. Selemon, L.D. (2013). A role for synaptic plasticity in the adolescent development of executive function. Transl Psychiatry *3*, e238. 10.1038/tp.2013.7.

42. Andrade-Talavera, Y., Fisahn, A., and Rodriguez-Moreno, A. (2023). Timing to be precise? An overview of spike timing-dependent plasticity, brain rhythmicity, and glial cells interplay within neuronal circuits. Mol Psychiatry. 10.1038/s41380-023-02027-w.

43. Fernandez-Ruiz, A., Sirota, A., Lopes-Dos-Santos, V., and Dupret, D. (2023). Over and above frequency: Gamma oscillations as units of neural circuit operations. Neuron *111*, 936-953. 10.1016/j.neuron.2023.02.026.

44. Paolicelli, R.C., Bolasco, G., Pagani, F., Maggi, L., Scianni, M., Panzanelli, P., Giustetto, M., Ferreira, T.A., Guiducci, E., Dumas, L., et al. (2011). Synaptic pruning by microglia is necessary for normal brain development. Science *333*, 1456-1458. 10.1126/science.1202529.

45. Schafer, D.P., Lehrman, E.K., Kautzman, A.G., Koyama, R., Mardinly, A.R., Yamasaki, R., Ransohoff, R.M., Greenberg, M.E., Barres, B.A., and Stevens, B. (2012). Microglia sculpt postnatal neural circuits in an activity and complement-dependent manner. Neuron *74*, 691-705. 10.1016/j.neuron.2012.03.026.

46. Borst, K., Dumas, A.A., and Prinz, M. (2021). Microglia: Immune and non-immune functions. Immunity *54*, 2194-2208. 10.1016/j.immuni.2021.09.014.

47. Roy, E.R., Chiu, G., Li, S., Propson, N.E., Kanchi, R., Wang, B., Coarfa, C., Zheng, H., and Cao, W. (2022). Concerted type I interferon signaling in microglia and neural

cells promotes memory impairment associated with amyloid beta plaques. Immunity *55*, 879-894 e876. 10.1016/j.immuni.2022.03.018.

48. Barrett, J.P., Henry, R.J., Shirey, K.A., Doran, S.J., Makarevich, O.D., Ritzel, R.M., Meadows, V.A., Vogel, S.N., Faden, A.I., Stoica, B.A., and Loane, D.J. (2020). Interferon-beta Plays a Detrimental Role in Experimental Traumatic Brain Injury by Enhancing Neuroinflammation That Drives Chronic Neurodegeneration. J Neurosci *40*, 2357-2370. 10.1523/JNEUROSCI.2516-19.2020.

49. Gulen, M.F., Samson, N., Keller, A., Schwabenland, M., Liu, C., Gluck, S., Thacker, V.V., Favre, L., Mangeat, B., Kroese, L.J., et al. (2023). cGAS-STING drives ageing-related inflammation and neurodegeneration. Nature. 10.1038/s41586-023-06373-1.

50. Mably, A.J., and Colgin, L.L. (2018). Gamma oscillations in cognitive disorders. Curr Opin Neurobiol *52*, 182-187. 10.1016/j.conb.2018.07.009.

51. Hu, J., Feng, X., Valdearcos, M., Lutrin, D., Uchida, Y., Koliwad, S.K., and Maze, M. (2018). Interleukin-6 is both necessary and sufficient to produce perioperative neurocognitive disorder in mice. Br J Anaesth *120*, 537-545. 10.1016/j.bja.2017.11.096.

52. Belarbi, K., Jopson, T., Tweedie, D., Arellano, C., Luo, W., Greig, N.H., and Rosi, S. (2012). TNF-alpha protein synthesis inhibitor restores neuronal function and reverses cognitive deficits induced by chronic neuroinflammation. J Neuroinflammation *9*, 23. 10.1186/1742-2094-9-23.

53. Arroyo-Garcia, L.E., Isla, A.G., Andrade-Talavera, Y., Balleza-Tapia, H., Loera-Valencia, R., Alvarez-Jimenez, L., Pizzirusso, G., Tambaro, S., Nilsson, P., and Fisahn, A. (2021). Impaired spike-gamma coupling of area CA3 fast-spiking interneurons as the earliest functional impairment in the App(NL-G-F) mouse model of Alzheimer's disease. Mol Psychiatry *26*, 5557-5567. 10.1038/s41380-021-01257-0.

54. Pizzirusso, G., Preka, E., Goikolea, J., Aguilar-Ruiz, C., Rodriguez-Rodriguez, P., Vazquez-Cabrera, G., Laterza, S., Latorre-Leal, M., Eroli, F., Blomgren, K., et al. (2024). Dynamic microglia alterations associate with hippocampal network impairments: A turning point in amyloid pathology progression. Brain Behav Immun *119*, 286-300. 10.1016/j.bbi.2024.04.009.

55. Emre, C., Arroyo-Garcia, L.E., Do, K.V., Jun, B., Ohshima, M., Alcalde, S.G., Cothern, M.L., Maioli, S., Nilsson, P., Hjorth, E., et al. (2022). Intranasal delivery of pro-resolving lipid mediators rescues memory and gamma oscillation impairment in App(NL-G-F/NL-G-F) mice. Commun Biol *5*, 245. 10.1038/s42003-022-03169-3.

56. Krukowski, K., Feng, X., Paladini, M.S., Chou, A., Sacramento, K., Grue, K., Riparip, L.K., Jones, T., Campbell-Beachler, M., Nelson, G., and Rosi, S. (2018). Temporary microglia-depletion after cosmic radiation modifies phagocytic activity and prevents cognitive deficits. Sci Rep *8*, 7857. 10.1038/s41598-018-26039-7.

57. Gibson, E.M., Nagaraja, S., Ocampo, A., Tam, L.T., Wood, L.S., Pallegar, P.N., Greene, J.J., Geraghty, A.C., Goldstein, A.K., Ni, L., et al. (2019). Methotrexate Chemotherapy Induces Persistent Tri-glial Dysregulation that Underlies Chemotherapy-Related Cognitive Impairment. Cell *176*, 43-55 e13. 10.1016/j.cell.2018.10.049.

58. Childs, B.G., Baker, D.J., Kirkland, J.L., Campisi, J., and van Deursen, J.M. (2014). Senescence and apoptosis: dueling or complementary cell fates? EMBO Rep *15*, 1139-1153. 10.15252/embr.201439245.

59. Suzuki, K., Ojima, M., Kodama, S., and Watanabe, M. (2003). Radiation-induced DNA damage and delayed induced genomic instability. Oncogene *22*, 6988-6993. 10.1038/sj.onc.1206881.

60. Gasek, N.S., Kuchel, G.A., Kirkland, J.L., and Xu, M. (2021). Strategies for Targeting Senescent Cells in Human Disease. Nat Aging *1*, 870-879. 10.1038/s43587-021-00121-8.

61. Sun, L., Wu, J., Du, F., Chen, X., and Chen, Z.J. (2013). Cyclic GMP-AMP synthase is a cytosolic DNA sensor that activates the type I interferon pathway. Science *339*, 786-791. 10.1126/science.1232458.

62. Gluck, S., Guey, B., Gulen, M.F., Wolter, K., Kang, T.W., Schmacke, N.A., Bridgeman, A., Rehwinkel, J., Zender, L., and Ablasser, A. (2017). Innate immune sensing of cytosolic chromatin fragments through cGAS promotes senescence. Nat Cell Biol *19*, 1061-1070. 10.1038/ncb3586.

63. Dou, Z., Ghosh, K., Vizioli, M.G., Zhu, J., Sen, P., Wangensteen, K.J., Simithy, J., Lan, Y., Lin, Y., Zhou, Z., et al. (2017). Cytoplasmic chromatin triggers inflammation in senescence and cancer. Nature *550*, 402-406. 10.1038/nature24050.

64. Tchkonia, T., Zhu, Y., van Deursen, J., Campisi, J., and Kirkland, J.L. (2013). Cellular senescence and the senescent secretory phenotype: therapeutic opportunities. J Clin Invest *123*, 966-972. 10.1172/JCI64098.

65. Cronk, J.C., Filiano, A.J., Louveau, A., Marin, I., Marsh, R., Ji, E., Goldman, D.H., Smirnov, I., Geraci, N., Acton, S., et al. (2018). Peripherally derived macrophages can engraft the brain independent of irradiation and maintain an identity distinct from microglia. J Exp Med *215*, 1627-1647. 10.1084/jem.20180247.

66. Shemer, A., Grozovski, J., Tay, T.L., Tao, J., Volaski, A., Suss, P., Ardura-Fabregat, A., Gross-Vered, M., Kim, J.S., David, E., et al. (2018). Engrafted parenchymal brain macrophages differ from microglia in transcriptome, chromatin landscape and response to challenge. Nat Commun *9*, 5206. 10.1038/s41467-018-07548-5.

67. Lund, H., Pieber, M., Parsa, R., Han, J., Grommisch, D., Ewing, E., Kular, L., Needhamsen, M., Espinosa, A., Nilsson, E., et al. (2018). Competitive repopulation of an empty microglial niche yields functionally distinct subsets of microglia-like cells. Nat Commun *9*, 4845. 10.1038/s41467-018-07295-7.

68. Dietrich, J., Baryawno, N., Nayyar, N., Valtis, Y.K., Yang, B., Ly, I., Besnard, A., Severe, N., Gustafsson, K.U., Andronesi, O.C., et al. (2018). Bone marrow drives central nervous system regeneration after radiation injury. J Clin Invest *128*, 2651. 10.1172/JCI121592.

69. Dyer, D.P., Medina-Ruiz, L., Bartolini, R., Schuette, F., Hughes, C.E., Pallas, K., Vidler, F., Macleod, M.K.L., Kelly, C.J., Lee, K.M., et al. (2019). Chemokine Receptor Redundancy and Specificity Are Context Dependent. Immunity *50*, 378-389 e375. 10.1016/j.immuni.2019.01.009.

70. Belarbi, K., Jopson, T., Arellano, C., Fike, J.R., and Rosi, S. (2013). CCR2 deficiency prevents neuronal dysfunction and cognitive impairments induced by cranial irradiation. Cancer Res *73*, 1201-1210. 10.1158/0008-5472.CAN-12-2989.

71. Zitvogel, L., Galluzzi, L., Kepp, O., Smyth, M.J., and Kroemer, G. (2015). Type I interferons in anticancer immunity. Nat Rev Immunol *15*, 405-414. 10.1038/nri3845.

72. Roughton, K., Kalm, M., and Blomgren, K. (2012). Sex-dependent differences in behavior and hippocampal neurogenesis after irradiation to the young mouse brain. Eur J Neurosci *36*, 2763-2772. 10.1111/j.1460-9568.2012.08197.x.

73. Vergara, R.C., Jaramillo-Riveri, S., Luarte, A., Moenne-Loccoz, C., Fuentes, R., Couve, A., and Maldonado, P.E. (2019). The Energy Homeostasis Principle: Neuronal Energy Regulation Drives Local Network Dynamics Generating Behavior. Front Comput Neurosci *13*, 49. 10.3389/fncom.2019.00049.

Figure legends

Figure 1: IR causes biphasic inflammatory waves in the hippocampus.

Also see Supplementary figure 1.

(A) Experimental design. SH, n = 6; IR, n = 6, per time point. h = hour, d = day, wk = week, P = postnatal, Hipp = hippocampus.

(B) Principal component analysis (PCA) plot showing distinct clustering of SH and IR samples in all studied time points.

(C) Bar plot showing the number of differentially expressed genes (DEGs) between SH and IR animals ($q < 0.05$). Positive y-axis indicates upregulated DEGs; negative y-axis indicates downregulated DEGs.

(**D - G**) Line graphs showing qPCR analyses of *Ifit1*, *Ifit3*, *Cxcl10* and *Ccl12* in the hippocampus across the studied time points. SH, n = 3-4; IR, n = 3-4. Mean ± SEM, unpaired *t*-test per time per time point to eliminate the animal age factor. $*p < 0.05$, $**p < 0.01$, $***p < 0.001$, $****p < 0.0001$.

(**H** and **I**) Line graphs showing ELISA measurements of the levels of CXCL10 and CCL12, respectively, in the hippocampus across the time post-IR. SH, n = 3-5; IR, n = 4-5. Mean ± SEM, unpaired *t*-test per timepoint. $*p < 0.05$, $**p < 0.01$.

Figure 2: Delayed microglial responses occurring at later phases post-IR.

Also see Supplementary figure 2.

(A) Experimental design. 2 wk, n = 4 per group; 6 wk, n = 3 per group.

(B) PCA plot showing distinct clustering of SH and IR samples at both time points.

(C) Left: Heatmaps depict DEGs ($q < 0.05$) between SH and IR microglia at 2 and 6 wk. Right: Venn diagram showing the number of distinct and overlapping DEGs between the two time points.

(**D** and **E**) Bar plots showing significantly regulated pathways ($q < 0.05$; red = upregulated; blue = downregulated) at 2 and 6 wk, respectively.

(**F**) Left: Representative confocal image displaying co-labeling of microglia (Iba1+, white) with Ki67 (red) in the *cornu ammonis* 1 (CA1) region of the hippocampus 2 wk post-IR. Hoechst (blue), nuclear counter stain. Scalebar = 10 μm. Middle and right panels: Quantification of $Iba1^{+}/Ki67^{+}$ in the molecular layer (ML) and CA1, respectively, across the studied time points. SH, n = 3-4; IR, n = 3-4. Mean ± SEM, unpaired *t*-test per time point. $*p < 0.05$, $****p < 0.0001$.

(**G**) Bar plots showing qPCR analyses of proinflammatory cytokines *Tnf* and *Il6* in the hippocampus 6 wk post-IR. SH, n = 4; IR, n = 4. Mean ± SEM, unpaired *t*-test. $*p < 0.05$.

Figure 3: The delayed post-IR microglial responses constitute multiple subpopulations. Also see Supplementary figures 3, 4, 5, and 6.

(A) Experimental design. SH, n = 3; IR, n = 3.

(B) Uniform manifold approximation and projection (UMAP) showing distinct clustering of hippocampal microglia from SH (blue) and IR (red) 2 wk post-IR.

(C) Microglial subclustering 2 wk post-IR revealed 12 subpopulations. Clusters 1, 3, 4, 6, 7, 9 and 10 were uniquely radiation-associated microglia (RAM) subpopulations.

(D) Dot plot showing the enriched pathways in RAM clusters ($p < 0.05$) 2 wk post-IR revealed by GSEA.

(E) RNA velocity analysis in RAM 2 wk post-IR showing that cells in cluster 6 are drivers for microglial mitotic progression. Arrow lengths indicate the speed of transcriptional activity.

(F) UMAP showing clustering of hippocampal microglia from SH (blue) and IR (red) 6 wk post-IR.

(G) Microglial subclustering 6 wk post-IR revealed 14 subpopulations. Clusters 2, 3, 4, 5, 7, 9, 10, 11 and 12 represent RAM.

(H) Dot plot showing the enriched pathways in the RAM clusters ($p < 0.05$) 6 wk post-IR revealed by GSEA.

I) RNA velocity analysis in RAM 6 wk post-IR showing RAM trajectories towards cluster 5.

Figure 4: The role of the cytoplasmic DNA sensing on the IFN response post-IR.

Also see Supplementary figure 7.

(A) Cell cycle analysis of proliferating RAM 2 wk post-IR.

(B) UMAPs showing expression of genes related to G2/M phase (*Cdk1*), DNA damage response (*Cdkn1a*), and IFN response (*Cxcl10*) in proliferating RAM 2 wk post-IR.

(C) *In vitro* experimental design. IF = immunofluorescence.

(D) Bar plots showing qPCR analyses of IFN-related genes *Ifit1*, *Ifit3*and *Cxcl10* in BV2 microglial cells 24 h post-IR. Three independent experiments. Mean ± SEM, unpaired *t*-test. $^{**}p < 0.01$, $^{***}p < 0.001$.

(E) Bar plot showing ELISA measurement of the levels of secreted CXCL10 in the culture media of BV2 microglial cells 24 h post-IR. Three independent experiments. Mean ± SEM, unpaired *t*-test. $^{*}p < 0.05$.

(F) Left: Representative confocal image displaying micronuclei and expression of cGAS (green; indicated by yellow arrows). Hoechst (blue), nuclear counter stain. Scalebar = 20 µm. Right: Bar plots showing the percentage of BV2 cells with micronuclei and cGAS expression 24 h post-IR. Three independent experiments. Mean ± SEM, unpaired *t*-test. $^{***}p < 0.001$, $^{****}p < 0.0001$.

(G) Left: Representative confocal image displaying expression of phosphorylated STING (pSTING; red; indicated by yellow arrows). Hoechst (blue), nuclear counter stain. Scalebar = 10 μm. Right: Bar plots showing the percentage of BV2 cells expressing pSTING 24 h post-IR. Three independent experiments. Mean ± SEM, unpaired *t*-test. $^{**}p < 0.01$.

(H) Bar plot showing the expression of phosphorylated TBK1 (pTBK1) in BV2 cells 24 h post-IR measured by immunoblotting. Three independent experiments. Mean ± SEM, unpaired *t*-test. $^{*}p < 0.05$.

Figure 5: Monocyte-derived macrophages (MDMs) infiltrate the hippocampus to compensate for the microglial loss post-IR.

Also see Supplementary figure 8.

(A) Experimental design. n = 3 per group.

(B) Heatmap depicts DEGs between SH and IR from bulk RNA-seq of the hippocampal tissue 6 mo post-IR.

(C) scRNA-seq of isolated $CX3CR1^{+}$ cells 6 mo post-IR Left: UMAP showing clustering of cells from SH (blue) and IR (red). Right: Subclustering revealed 11 distinct clusters. RAM in cluster 1 remained distinct from SH and other IR microglia.

(D) UMAPs showing expression of signature genes of microglia (*Sall1*) and MDMs (*Ms4a7*) in RAM 6 mo post-IR.

(**E**) RNA velocity analysis in RAM 6 mo post-IR revealed that MDMs display trajectories towards parenchymal microglia.

(**F**) Left: Representative confocal images displaying co-labeling of $Iba1^{+}$ cells (green) $Tmem119^{+}$ (red) in the CA1 6 mo post-IR. Hoechst (blue), nuclear counter stain. Arrows indicate $Tmem119^{low}$ and arrow heads indicate $Tmem119^{high}$. Scalebar = 50 μm (overview) and = 10 μm (closeup). Right: Bar plot showing quantification of $Tmem119^{low}$ or

Tmem119^{negative} cells in the CA1 6 mo post-IR. SH, n = 3; IR, n = 3. Mean ± SEM, unpaired *t*-test. *$p < 0.05$, **$p < 0.01$.

(G) Line graph showing the quantification of Iba1^{+} cells in CA1 region across time post-IR. n = 3-5 per group. Mean ± SEM, unpaired *t*-test per time point. *$p < 0.05$, **$p < 0.01$, ***$p < 0.001$.

(**H**) Experimental design for assessing microglial survival.

(**I**) Left: Representative confocal image displaying co-labeling of microglia (Tmem119^{+}, green) with BrdU (red) in the CA1 2 wk post-IR. Hoechst (blue), nuclear counter stain. Scalebar = 10 μm. Right: Bar plot showing quantification of Tmem119^{+}/BrdU^{+} cells 2 wk and 6 wk post-IR in the CA1. 2 wk, n = 4-5; 6 wk, n = 5. Mean ± SEM, two-way ANOVA with Bonferroni's *posthoc* for multiple comparisons. **$p < 0.01$, ****$p < 0.0001$.

Figure 6: MDMs ensue infiltering the brain at an early phase post-IR.

Also see Supplementary figures 9, 10, 11, and 12.

(**A**) UMAP showing the dynamic of IR-induced MDM (iMDM) clusters over the time post-IR.

(**B**) Top: UMAP combining iMDM clusters from 2 wk, 6 wk and 6 mo. Bottom: CellRank-Moscot analysis revealed that iMDMs from 2 and 6 wk (black dots) are the initial state, and cells in 6 mo (yellow dots) are the terminal state.

(**C**) Left: UMAPs showing *Tmem119* expression in iMDMs over the time post-IR. Right: Dot plot showing magnitude of *Tmem119* expression in the iMDM clusters.

(**D**) Heatmap showing expression of chemokine receptors in the iMDM clusters.

(**E**) Representative confocal images displaying expression of IBA1$^+$ cells (green) TMEM119$^+$ (red) in cancer-free hippocampus of a medulloblastoma patient 5 years post-radiotherapy. Yellow arrows indicate Iba1$^+$/Tmem119^{low} cells. Hoechst (blue), nuclear counter stain. Scale bar = 20 μm.

(**F**) Experimental design. yr = Year. n = 3 per group.

(**G**) UMAP showing clustering of hippocampal microglia from SH (blue) and IR (red) 1 yr post-IR.

(**H**) UMAPs showing subclustering of hippocampal microglia 1 yr post-IR. Thirteen clusters were revealed, of which some were enriched (clusters 5 and 7) or repressed (cluster 6) post-IR.

(I) Bar plot showing quantification of Iba1$^+$ cells in the CA1, 1 yr post-IR. SH, n = 5; IR, n = 5. Mean ± SEM, unpaired *t*-test per time point. $^{**}p < 0.01$.

(**J**) Bar plots showing qPCR analyses of inflammatory mediators *Ifit1*, *Cxcl10* and *Il6* in the hippocampus 1 yr post-IR. SH, n = 4-5; IR, n = 5. Mean ± SEM, unpaired *t*-test. $^{*}p < 0.05$.

Figure 7: Longitudinal overview of RAM and the hippocampal neuronal network synchrony.

Also see Supplementary figure 13.

(A) UMAP showing clustering of microglia collected from age-matched SH controls from 6 h to 1 yr time points.

(**B**) UMAP showing clustering of RAM from 6 h to 1 yr.

(**C**) CellRank-Moscot analysis on SH microglia over time visualizing the initial state (6 h, black dots) and the terminal state 1 yr (yellow dots).

(**D**) CellRank-Moscot analysis on RAM over the time post-IR visualizing the initial state (6 h, black dots), intermediate state (2 wk), and the terminal states (6 wk, 6 mo and 1 yr, yellow dots).

(**E**) Representative diagram of electrode location in area CA3 of hippocampal slices.

(**F**) Representative sample traces of local field potentials (LFP) recordings from SH and IR slices 2□wk, 6□wk, 6□mo and 1 yr. SH, n = 3-5; IR, n = 3-5, per time point.

(**G**) Representative power spectra of hippocampal CA3 network activity recorded in SH and IR slices 2□wk, 6□wk, 6□mo and 1 yr.

(**H**) Gamma oscillation power post-IR. Mean ± SEM, unpaired *t*-test per time point to eliminate the animal age factor. *$p < 0.05$, **$p < 0.01$, ***$p < 0.001$.

(**I**) Frequency variance at the above-mentioned time points after IR. Mean ± SEM, unpaired t-test. *$p < 0.05$.

Supplementary figures

Supplementary figure 1: IR causes biphasic inflammatory waves in the hippocampus. Related to Figure 1.

(**A**) Bar plot showing significantly enriched pathways ($p < 0.05$) 2 wk post-IR revealed by geneset enrichment analysis (GSEA).

(B and C) Bar plots showing expression of 14 inflammation-related genes in the hippocampus 2 weeks (wk) post-IR ($q < 0.05$), 12 were belonging to IFN signaling pathways (**B**). FPKM = fragments per kilobase of transcript per million fragments mapped.

(D) Heatmaps depicts profiling of chemokines and chemokine receptors in the hippocampus across the time post-IR. SH, n = 6; IR, n = 6, per time point. *$p < 0.05$, **$p < 0.01$.

(**E**) Line graphs showing ELISA measurements of the levels of CCL2 in the hippocampus across the time post-IR. SH, n = 3-5; IR, n = 3-5. Mean ± SEM, unpaired *t*-test per timepoint. **$p < 0.01$, ***$p < 0.001$, ****$p < 0.0001$.

Supplementary figure 2: Delayed microglial responses occurring at later phases post-IR Related to Figure 2.

(A) Heatmaps depict significantly regulated genes related to cytokines and chemokines in isolated microglia 2 wk (left) and 6 wk (right) post-IR.

(B) Representative confocal images displaying co-labeling of microglia (Iba1+ in green) and oligodendrocytes progenitors (Olig2$^+$; white) with the cell cycle marker Ki67 (red) in the molecular layer (ML) of the hippocampus 2 wk post-IR. Hoechst (blue), nuclear counter stain. Scalebar = 10 µm.

(C) Line graphs showing the quantification total of Ki67$^+$ cells in the ML (left) and *cornu ammonis* 1 (CA1) region (right), across the time post-IR. SH, n = 3-4; IR, n = 3-4. Mean ± SEM, unpaired *t*-test per time point. *$p < 0.05$, ***$p < 0.001$.

(D) Line graphs showing percentage Olig2$^+$ cells of total Ki67$^+$ cells in the ML and CA1, across the time post-IR. SH, n = 3-4; IR, n = 3-4. Mean ± SEM, unpaired *t*-test per time point. ***$p < 0.001$, ****$p < 0.0001$.

(E) Line graphs showing percentage Iba1$^+$ cells of total Ki67$^+$ cells in the ML and CA1 across the time post-IR. SH, n = 3-4; IR, n = 3-4. Mean ± SEM, unpaired *t*-test per time point. *$p < 0.05$, ***$p < 0.001$, ****$p < 0.0001$.

(F) Line graphs showing quantification of the proliferating oligodendrocyte progenitors ($Olig2^+/Ki67^+$) in the ML and CA1 across the studied time points post-IR. SH, n = 3-4; IR, n = 3-4. Mean ± SEM, unpaired *t*-test per time point. $*p < 0.05$, $**p < 0.01$.

(**G**) Bar plot showing qPCR analysis of proinflammatory chemokine *Cxcl2* in the hippocampus 6 wk post-IR. SH, n = 4; IR, n = 4. Mean ± SEM, unpaired *t*-test. $*p < 0.05$.

Supplementary figure 3: scRNA seq 2 wk post-IR. Related to Figure 3

(**A**) Uniform manifold approximation and projection (UMAP) showing clustering of the cell types captured using our cell isolation protocol from SH and IR hippocampi 2 wk post-IR. n = 3 per group.

(**B**) UMAP showing the cell types in SH (blue) and IR (red) animals.

(**C**) Bar plot showing the number of DEGs in all captured cell types.

(**D**) Violin plots showing expression of *Cxcl10* (top) and *Ccl12* (bottom) per cell type post-IR.

(**E**) UMAPs showing that expression of the IFN-related genes *Ifit1*, *Ifit3* and *Cxcl10* mainly was in cluster 6, and the expression of the cell cycle genes *Mki67* and *Top2a* was in clusters 7, 9 and 10 of RAM 2 wk post-IR.

Supplementary figure 4: Enriched pathways in RAM 2 wk post-IR. Related to Figure 3.

(**A**) Dot plots showing the activated and suppressed pathways in the RAM clusters 2 wk post-IR revealed by GSEA.

Supplementary figure 5: Enriched pathways in RAM 6 wk post-IR. Related to Figure 3.

(**A**) Dot plots showing the activated and suppressed pathways in the RAM clusters 6 wk post-IR revealed by GSEA.

Supplementary figure 6: *Tnf* and *Il6* expression in RAM 6 wk post-IR. Related to Figure 3.

(**A** and **B**) UMAPs showing expression of *Tnf*, and *Il6* in RAM 6 wk post-IR.

Supplementary figure 7: The role of the cytoplasmic DNA sensing on the IFN response post-IR. Related to Figure 4.

(A) Representative confocal image displaying expression of the DNA damage response marker γH2AX (red) in the nuclei (Hoechst, blue) of BV2 microglial cells 1 h post-IR. Scalebar = 10 μm.

Supplementary figure 8: Microglial loss and MDM infiltration into the hippocampus. Related to Figure 5.

(A) UMAPs showing the expression signature genes of microglia (*Tmem119* and *Slc2a5*) and MDMs (*Clec12a* and *Itga4*) in RAM 6 mo post-IR.

(B) Upper panel: UMAPs showing clustering of unsorted hippocampal microglia from SH (blue) and IR (red) 6 mo post-IR. Subclustering revealed 12 clusters. Lower panel: UMAPs showing the expression of *Sall1* (microglia) and *Ms4a7* (MDMs). Cells in cluster 6 represents MDMs.

(C) UMAPs displaying expression of the microglial signature gene *Sall1* and MDM signature gene *Ms4a7 in* RAM 6 mo post-IR where RNA velocity analysis was applied.

(D) Dot plots showing morphological comparisons between the Tmem119^{high} and Tmem119^{low} cells 6 mo post-IR. n = 144 - 229 cells collected from n = 3 animals per group. Mean ± SEM, unpaired *t*-test. ****$p < 0.0001$.

(E) Bar plots showing quantification of total BrdU^{+} cells (left) and percentage of Tmem119^{+} of total BrdU^{+} cells (right) in the CA1 2 and 6 wk post-IR. 2 wk, n = 4-5; 6 wk, n = 5. Mean ± SEM, two-way ANOVA with Bonferroni's *posthoc* for multiple comparisons. **$p < 0.01$, ***$p < 0.001$, ****$p < 0.0001$. ns = not significant.

(**F**) Bar plots showing qPCR analyses of proinflammatory mediators in the hippocampus 6 mo post-IR. SH, n = 4; IR, n = 4. Mean ± SEM, unpaired *t*-test. ns = not significant.

Supplementary figure 9: MDM dynamics over the time post-IR. Related to Figure 6.

(**A**) UMAP showing the macrophage populations detected in the hippocampus of SH and IR animals. IR-induced MDMs (iMDMs) were cluster 1 (= iMDM1 in Figure 6A), 2 (= iMDM2), and 5 (= iMDM3).

(**B**) Stack plot showing the proportion of iMDMs clusters over the time post-IR.

(**C**) Bar plot showing quantification of Iba1^{+}/ Tmem119^{negative} in the CA1 6 wk post-IR. SH, n = 4; IR, n = 4. Mean ± SEM, unpaired *t*-test. *$p < 0.05$.

(**D**) UMAPs visualizing the probabilities of the initial and terminal states among the iMDMs.

(**E**) Comparisons between the Iba1^{+}/Tmem119$^{negative\ and\ low}$ cells detected 6 wk and 6 mo post-IR. Left: Representative confocal images displaying co-labeling of Iba1^{+} cells (green) Tmem119^{+} (red) in the CA1 at both time points. Hoechst (blue), nuclear counter stain. Arrows indicate Tmem119^{low}, and arrow heads indicate Tmem119^{negative}. Scalebar = 10 μm. Left: Quantification of the number of processes per cell. n = 74 -141 cells collected from n = 3 - 4 animals per group. Mean ± SEM, unpaired *t*-test. ****$p < 0.0001$.

(**F**) Bar plot showing quantification of Iba1^{+}/ Tmem119^{negative} in CA1 of *Ccr2* knockout (KO) mice 6 wk post-IR. SH, n = 3; IR, n = 4. Mean ± SEM, unpaired *t*-test. *$p < 0.05$.

Supplementary figure 10: Comparison of iMDMs with blood or CNS-associated bone marrow-derived MDMs. Related to Figure 6.

(**A**) UMAP showing embedding of the 6-wk iMDMs post-IR with the monocytes/macrophages/microglia population presented in scRNA-seq from (Cugurra *et al.*, 2021) derived from the blood (Cugurra GFP) or CNS-associated bone marrow (Cugurra WT).

B) Subclustering of the cells in (**A**).

(**C**) Visualization of *Ccr2* expressing cells in each population.

Supplementary figure 11: Validation of immunofluorescence staining in human samples. Related to Figure 6.

(A and **B**) Representative confocal images showing validation of immunofluorescence staining for expression of IBA1^{+} (green) TMEM119^{+} (red) cells in human brain tissues. (**A**) Showing colocalization of IBA1 and TMEM119 in postmortem hippocampal tissue donated by a 54-year-old healthy male (positive control for both staining). (**B**) Showing IBA1^{+} /TMEM119^{negative} macrophages infiltrating a surgically resected ependymoma tissue (positive control for IBA1 and negative control for TMEM119). Hoechst (blue), nuclear counter stain. Scale bar = 20 μm.

Supplementary figure 12: The microglial alterations and the inflammatory response 1 yr post-IR. Related to Figure 6.

(**A**) Dot plot showing the enriched pathways 1 yr post-IR in SH (Left) or RAM (right) revealed by GSEA.

(B) UMAPs showing expression of the microglia signature genes *Sall1* and the MDM signature gene *Ms4a7*.

(**C**) Bar plots showing qPCR analyses of inflammatory mediators *Ifit3*, *Ccl12* and *Tnf* in the hippocampus 1 yr post-IR. SH, n = 5; IR, n = 5. Mean ± SEM, unpaired *t*-test. ns = not significant.

(**D**) Heatmap showing average expression of the cytokines, chemokines and their receptors detected in each microglial cluster from SH and RAM 1 yr post-IR.

Supplementary figure 13: Integration of microglia across the time points. Related to Figure 7

(**A**) UMAPs showing expression of the IFN-related genes *Ifit3* and *Cxcl10* and the cell cycle-related genes *Mki67* and *Top2a* in intermediate (2 wk) RAM.

Materials and methods

Animals

Female mice were used in all studies, as irradiation (IR)-induced cognitive deficits are more severe in females, both in animal models and patients [2,72]. Twenty-one- or twenty-five-day-old mice of the following strains were used C57BL/6J (Charles River, Sulzfeld, Germany, stock #000664), B6.129(Cg)-*Ccr2*tm2.1Ifc/J (*Ccr2*^{RFP}) (Jackson laboratory; stock #017586). Animals were housed in equal light/dark cycles (12/12 h) and were fed *ad libitum*. All the experimental procedures were carried out according to the European and Swedish animal welfare regulations approved by the northern Stockholm ethical committee (application nr. N248/13, N141-16 and 13676-2020).

Irradiation procedure

Mice were initially anesthetized with 5% isoflurane in an induction chamber in a mixture of air and oxygen (1:1), then transferred to the irradiation machine and placed in a prone position. The anesthesia was maintained with 1.5 % isoflurane during the irradiation procedure. The following irradiation machines were used: X-RAD 320 (PXi Precision X-ray, North Branford, CT, USA) or CIX3 cabinet x-ray irradiator (XStrahl, Surrey, England). For the X-RAD 320 irradiator, the animal head was distanced approximately 50 cm from the radiation source, and an irradiation field of 2 × 2 cm was used to cover the entire head. Animals received a single dose of 8 Gy delivered at a rate of 0.73 Gy/min. For the Xtrahl irradiator, the animal head was irradiated with a circular field of 1.5 cm in diameter. The collimator was an XStrahl Perspex tip applicator. A single dose of 8 Gy was delivered with a dose rate of 1.349 Gy/min (dosimetry uncertainty ~ 2%) at 300 kV and 10 mA. Focus skin distance (FSD) to the animal head was 32 cm. External filtration giving a half-value layer (HVL) of 4.0738 mm Cu was applied by adding a Thoraeus filter (1.0 mm Sn, 0.25 mm Cu, 1.50 mm Al). Litter-mates sham controls (SH) were subjected to the same duration of

anesthesia in the absence of IR. Animals were allowed to recover from the anesthesia and returned to their cages.

5-bromo-2'-deoxyuridine (BrdU) administration

To assess survival of proliferating microglia, dividing cells were labeled between day 10 and 13 post-IR with the thymidine analog BrdU (SigmaAldrich #B5002). BrdU was injected i.p. at a dose of 50 mg/kg, two injections per day (6 h apart). Animals were sacrificed either 2 h or 4 weeks after the last BrdU injection to assess proliferation and survival of the newborn cells, respectively.

Tissue collection

Animals were sacrificed at 6 hours, 1 day, 1 week, 2 weeks, 6 weeks, 6 months, or 1 year post-IR. Animals were deeply anesthetized with sodium pentobarbital (100 mg/kg, ABCUR AB #444362, Sweden), and transcardially perfused with 1× phosphate-buffered saline (PBS; ThermoFisher Scientific #10010023). Brains were collected and the hemispheres were separated. The left hemispheres were placed into 4% paraformaldehyde (PFA; Histolab Products # HL96753.1000, Sweden) and stored at 4 ºC for 48 h. The brains were then cryoprotected in 30% sucrose solution (Sigma-Aldrich #S7903) made in 0.1 M phosphate buffer pH 7.4 and stored at 4 ºC until slicing. Right hemisphere hippocampi were dissected and kept in a -80 ºC freezer until further processing for RNA or protein extraction.

Generation of single-cell suspension for RNA sequencing

Single-cell suspensions were prepared from three SH controls and three IR mice per time point. Animals were deeply anesthetized with sodium pentobarbital (100 mg/kg, ABCUR AB, Sweden) and transcardially perfused with ice-cold 1× PBS without $Ca^{2+}$and Mg^{2+}(PBS; pH 7.4; Gibco/Life Technologies #10010056). Brains were collected and the hippocampi from

the two hemispheres were dissected and put into 1.5 mL eppendorf tubes containing 1× PBS placed on ice. The tissue was chopped into small pieces using scalpel and transferred into conical tubes containing an enzymatic mixture of Dispase II (0.01%; Sigma-Aldrich #D4693), papain (0.1%; Roche #000000010108014001) and DNaseI (0.05%; Roche # 000000010104159001) in 1× Hank's buffered salt solution (HBSS) without $Ca^{2+}$and Mg^{2+} (Gibco/Life Technologies #14175095), later supplemented with 12.4 mM magnesium sulfate (Sigma-Aldrich #M7506). Tubes were incubated at 37ºC for 10 min, after which the enzymatic activities were stopped with 20% ice-cold heat-inactivated fetal bovine serum (FBS; Gibco/Life Technologies #10500064). The cell suspension was then filtered through a 70 μm cell strainer and centrifuged for 5 min at 500 g at 4 ºC. After washing with 1× HBSS, cells were resuspended in 20% percoll solution (percoll plus, GE Healthcare, #GE17-0891-02); 10× phenol red HBSS (Gibco/Life Technologies #14060040) and 1× HBSS, and overlaid with an equal volume of 1× HBSS. Tubes were spun at 1,000 × g at 4ºC for 30 min with no break to remove myelin. The cell pellet was resuspended in 1 ml flow cytometry buffer (R&D Systems #FC001). In protocols intended to collect neurons, an additional centrifugation step in a higher percoll concentration was applied. The supernatant from the first percoll step (20 %) was collected in 50 ml conical tubes and mixed with an equal volume of 50 % percoll solution to obtain a concentration of 30 % percoll, and spun at 1,000 × g at 4ºC for 30 min with a break. The supernatant was removed, and the pellet was resuspended in 1 ml flow cytometry buffer. Both cellular fractions collected from the two-step percoll were mixed and spun at 500 × g at 4 ºC for 5 min. The pellet was resuspended in 0.5 ml flow cytometry buffer. Cells processed for single-cell RNA-seq were pooled from three SH and three IR animals before adding the flow cytometry buffer and processed for 10× single-cell RNA sequencing. For the sorted microglia, only the first percoll step was applied to get the cell suspension that contained the microglial fraction. That cell suspension was incubated

with a Fc-blocker (Miltenyi # 130-092-575) for 10 min, followed by incubation with a PE-conjugated goat anti-CX3CR1 antibody (R&D Systems #FAB5825P) for 15 min. SytoxRed (Invitrogen #S11381) was used as a live/dead cell stain. Cells were sorted using FACSAria III (BD Biosciences, New Jersey, USA) into a 1.5 ml eppendorf tube containing 0.5 ml flow cytometry buffer and placed on ice, when processed for 10×single-cell RNA-seq, or a 1.5 mL eppendorf tube containing 0.25 ml Qiazol (Qiagen #79306) and placed on dry ice, then stored -80 ºC. For each time point, cells were isolated from SH and IR animals at the same time and processed in the same manner (as one batch).

RNA isolation and Quantitative real-time polymerase chain reaction (qPCR):

RNA was isolated from the BV2 cells using the RNeasy Plus Micro Kit (Qiagen, #74034), from tissue using the RNeasy Plus Mini Kit (Qiagen, #74134), and from sorted cells using the miRNeasy Micro Kit (Qiagen, #217084). cDNA was generated using the QuantiTect® Reverse Transcription Kit (Qiagen, #205311) using the AB Simpliamp Thermal PCR machine (Applied Biosystems). The qPCR was performed using the QuantiTect SYBR Green PCR Kit (Qiagen, #204143). Target mRNA expression was assessed using the QuantiTect primer assay (Qiagen). The following primers were used: Mm_*Gapdh*_3_SG (#QT01658692); Mm_*Ifit1*_1_SG (#QT01161286); Mm_*Ifit3*_1_SG (#QT00292159); Mm_*Cxcl10*_1_SG (#QT00093436); Mm_*Ccl12*_1_SG (#QT00244391); Mm_*Tnf*_1_SG (QT00104006); Mm_*Il6*_1_SG (#QT00098875); Mm_*Cxcl2*_1_SG (QT0011325). qPCR was performed using either the StepOnePlus™ Real-Time PCR System (Applied Biosystems #4376600) or the CFX384 Touch Real-Time PCR Detection System (Bio-rad #1855484). Relative mRNA expression was determined using the $^{\Delta\Delta}$CT method, and *Gapdh* was used as a housekeeping gene.

Bulk RNA sequencing:

Isolated RNA was processed for sequencing at the Bioinformatics and Expression Analysis core facility (BEA) at Karolinska Institutet, Sweden or at BGI Genomics, China. For sequencing of RNA isolated from the whole hippocampus tissue, the total RNA was subjected to quality control with Agilent Tapestation according to the manufacturer's instructions. 200 ng of total RNA were subjected to Illumina sequencing, and libraries were prepared with the Illumina TruSeq Stranded mRNA ligation prep kit, which includes cDNA synthesis, ligation of adapters and amplification of indexed libraries. The yield and quality of the amplified libraries were analyzed using Qubit by Thermo Fisher and the Agilent Tapestation. The indexed cDNA libraries were normalized and combined, and the pools were sequenced on the Illumina Nextseq 550 using a V2.5 75-cycle flowcell generating 75 bp single-end reads. Basecalling and demultiplexing were performed using BCL2 software with default settings generating Fastq files for further downstream mapping and analysis. For sequencing of RNA isolated from sorted microglia at 2 and 6 wk post-IR, the RNA quality was checked on an Agilent bioanalyzer 2100 using the Eukaryote total RNA picochips, and library preparation was performed using QIAseq FX single-cell RNA library kit (QIAGEN), then sequenced on an Illumina HiSeq 2000. For data analysis, unsupervised hierarchical clustering and principal component analyses (PCA) were performed in Qlucore Omics Explorer 3.2 (Qlucore, Lund, Sweden). Differentially expressed genes were determined by comparing irradiated- and sham-treated animals using heteroscedastic two-tailed *t*-tests. Multiple testing correction was performed using the Benjamini-Hochberg algorithm with a false discovery rate (FDR) of 5 %.

For gene set enrichment analysis, ranked gene lists were prepared based on signal to noise ((Mean radiated - mean sham)/sum of standard deviations). Human gene names were utilized for input of ranked gene lists into the GSEA application https://www.gsea-msigdb.org/gsea/index.jsp, Broad Institute, Inc), using the GSEAPreranked tool.

Single-cell RNA sequencing

Isolated cells were processed for single cell RNA sequencing at the eukaryotic single-cell genomics facility (ESCG) at Karolinska Institutet, Sweden using the 10× Genomics Chromium method (version 3) and sequenced using Illumina NovaSeq 6000 on an S1, S2 or S4 flow cell. The Cellranger 6.0.1 pipeline was used to align the raw sequencing reads to the mouse reference genome, *Mus musculus* version *mm10,* and generate the unique molecular identifier (UMI) count matrix. The generated count matrix was analyzed using the Seurat R package (version 3.0.0). Each condition included 3 technical replicates, and each replicate was processed independently before integration. Low-quality cells were excluded based on the number of genes expressed in the cells and the percentage of mitochondrial counts. Cells expressing a minimum of 250 genes and a maximum of 6,000 genes were considered for downstream analysis, given that each gene was expressed in at least three cells. The hippocampal cellular components are heterogeneous, and each cell type has a different energy demand, with neurons having the highest energy consumption [73]. To ensure inclusion of all cell types, the threshold for the mitochondrial counts was set at 45%. The filtered count matrices were normalized by dividing the feature counts for each cell by the total number of counts from all cells, then multiplied by 10,000 and log-transformed. Next, we identified highly variable features for each dataset independently. We used the default Seurat method for the integration of datasets and removal of the batch effect. In brief, we used canonical correlation analysis and identified “anchors” (conserved cell groups) between datasets, which were used for batch correction and for the comparison of the differentially expressed genes

between experimental conditions. The data were scaled using Pearson residuals, regressing out the variation by the mitochondrial genes. PCA was then performed on the scaled data for the dimensionality reduction, using 30 components. The output was used to produce a Uniform Manifold Approximation and Projection for Dimension Reduction (UMAP) with a resolution of 0.5 for identification of the clusters. After quality control, a total of 126,041 single cells collected from the 2 week, 6 week, 6 months and 1 year time points were analyzed. Cell numbers per condition per time point per experimental condition were: two-week all cell types: SH: 26,531; IR: 26,560. Two-week microglia: SH: 8,149; IR: 7,988. Six-week microglia: SH: 4,107; IR: 10,099. Six-months microglia (CX3CR1 sorted): SH: 2,170; IR: 3,514. Six months microglia (unsorted): SH: 5,940; IR: 8,190. One-year microglia: SH 11,292; IR: 11,501. Identification of each cluster was based on signature genes of each cell type according to the existing literature as well as through the automatic cell type recognition package SingleR. Signature genes for microglia included *Sall1*, *Cx3cr1*, *P2ry12*; for macrophages *Mrc1* and *Ms4a7*; for oligodendrocytes, *Pdgfra*, *Olig2* and *Mog*; for astrocytes *Gja1* and *Aqp4*; for neurons *Dcx*, *Rbfox3* and *Syt1*; for endothelial cells *Cldn5*; for pericytes *Vtn* and *Pdgfrb*; for fibroblasts/myofibroblasts *Col1a1* and *Acta2*. The proliferating cells were identified using markers such as *Mki67* and *Top2a*. As we focused on microglia, the microglial cells from all studied time points were selected and undergone the above-mentioned quality control step, except that the mitochondrial counts were set to 10%. Cells were then subclustered and analyzed in-depth.

ClusterProfiler package was used for gene set enrichment analysis of the upregulated and statistically significant differentially expressed genes (DEGs) of the microglial clusters from each time point. Highly expressed and unique genes for each cluster that were expressed by at least 30-50% of the cells were included.

Scoring of the cell cycle phases of each cell was calculated using the CellCycleScoring function in the Seurat pipeline, based on a set of genes expressed during the S and G2/M phases. The assigned scores for the S and G2/M phases were saved on the metadata of the Seurat object.

For the estimation of the RNA velocity, the post-alignment bam files were used to run velocyto command v0.17, *run* for any technique. To mask the potential repeats of expressed genes, we retrieved the mouse repeat annotation file from the UCSC genome browser (mm10_rmsk.gtf). The mouse genome annotation reference was acquired from CellRanger, and the resultant loom files contained the spliced and unspliced counts. The scVelo tool was used to estimate the generalized RNA velocity model. We extracted the coordinates, count matrix, and gene names of the processed Seurat object for microglia from R and created an anndata object. The obtained loom file and the anndata object were merged, and the generalized dynamical model was used for the velocity estimation and plotting of velocities.

The Moscot/Cellrank module was used to examine the development of the cells across experimental time points. According to the default procedure of Moscot to perform time series data analysis, we set up a temporal problem, which matched cells coming from different time points using the method of optimal transport (OT)[37]. A kernel (RealTimeKernel) was created to compute the transition matrix using a connectivities' self-transitions weight of 0.2. We passed the RealTimeKernel to the Generalized Perron Cluster Cluster analysis (GPCCA) estimator to estimate and classify macrostates into initial, intermediate, and terminal states. The predicted initial states were used to infer cellular dynamics by calculating absorption probabilities, which were visualized in the form of random walks.

Cell culture

The murine microglia cell line BV2 was used. Cells were cultured in DMEM GlutaMAX (GIBCO/Life Technologies #10564011) with 10% FBS and 5% penicillin/streptomycin. Cells were grown at 37°C in 5% CO_2, split and passaged every 2 - 3 days. For irradiation, BV2 cells were seeded in 6-well plates at a density of 1.5×10^5 and allowed to settle overnight. Cells were irradiated on the CIX2 X-ray irradiator (XStrahl, Surrey, England) with a single dose of 8 Gy delivered at a rate of 1.35 Gy/min. A rotating platform was used to ensure homogenous dose delivery. Control cells were positioned in the rotating platform for a similar amount of time required to deliver 8 Gy without IR. BV2 cells or culture media were collected 1 h or 24 h post-IR. The culture media were spun for 10 min at 4°C at 10,000 × g, and the supernatants were transferred into 1.5 ml tubes and stored at -80°C. The cells were washed with 1× PBS, and the following buffers were added depending on the intended downstream analysis: Loading buffer (for western blot), RLT buffer + β-mercaptoethanol (for qPCR) or ice-cold 4% PFA (for immunostaining) were added to the wells and samples were collected with a cell scraper and a pipette.

Immunohistochemistry and immunofluorescence

For mouse brain tissues, the left hemispheres were cut sagittally into 25-μm-thick free-floating sections made in 1:12 series intervals using a sliding microtome (Leica SM2010R) and stored in 2 ml eppendorf tubes containing a cryoprotectant solution (25% glycerol, 25% ethylene glycol in 0.1M phosphate buffer) and kept at +4°C. After several washes with 1× Tris-buffered saline (TBS), samples were incubated in sodium citrate solution (NaCi, 10 mM, pH 6.0) for 30 min at 80°C when antigen retrieval was needed. When immunoperoxidase staining used, sections were incubated in a 0.6% hydrogen peroxide (H_2O_2) solution for 30 min to quench the endogenous peroxidase. For BrdU staining, the double-stranded DNA denatured by incubating the sections in 2 N HCl at 37°C for 30 min followed by a

neutralization step performed by incubating the section in a 0.1 M borate buffer for 10 min at room temperature. Sections were washed with TBS. Non-specific binding was blocked by incubating the sections in a solution of 3% or 5% normal donkey serum (Jackson ImmunoResearch Laboratories; #017000121), 0.1% Triton X-100 (made in TBS) for 1 h at room temperature. Sections were then incubated with primary antibodies at 4ºC for 24 - 72 h, depending on the antibody. The following primary antibodies were used: goat anti-Iba1 (Abcam# ab5076; 1:500); rabbit anti-Iba1 (Wako Chemicals #1919741; 1:1,000); rabbit anti-Tmem119 (Abcam #ab209064; 1:500); rat anti-Ki67 (ThermoFisherScientific #14-5698-82; 1:500); goat anti-Olig2 (R&D Systems #AF2418; 1:500); rat anti-BrdU (Abcam #6326; 1:500). Sections were incubated for 1 h or 2 h at room temperature with appropriate biotinylated or fluorescent secondary antibodies, respectively. The following secondary antibodies were used: Biotinylated donkey anti-goat IgG (Jackson ImmunoResearch #705-065-147; 1:1,000); AlexaFlour-488 donkey anti-goat IgG (Molecular probes/Life Technologies #A11055; 1:1,000); AlexaFlour-488 donkey anti-mouse IgG (Molecular probes/Life Technologies #A21202; 1:1,000); AlexaFlour-555 donkey anti-rabbit IgG (Molecular probes/Life Technologies #A31572; 1:1,000); AlexaFlour-555 donkey anti-rat IgG (Abcam #ab150154; 1:1,000); CF-633 donkey anti-goat IgG (Biotium #20127; 1:1,000). To visualize the immunoperoxidase staining, sections were incubated for 1 h at room temperature in avidin-biotin solution (Vectastain ABC Elite kit, Vector Laboratories #PK6100, Burlingame, CA; 1:100). The color precipitate was developed with a solution containing H_2O_2, nickel chloride, and 3-3´diaminobenzidine tetrahydrochloride (DAB; 1:100; Saveen Werner AB, Malmö, Sweden). Sections were mounted into slides, dehydrated with NeoClear (Merck #1.09843.5000, Germany) and coverslipped using NeoMount mounting medium (Merck #1.09016.0500, Germany).

For human tissues, sections were deparaffinized using xylene, rehydrated in descending ethanol series (100 - 70%), and then washed with 1× TBS. Antigen retrieval was performed by heating the section in a solution containing 10 mM Trisma base (Sigma-Aldrich), 1 mM ethylenediaminetetraacetic acid (EDTA; Merck-Millipore) and 0.05% tween-20 (Merck-Millipore), pH 9. Non-specific binding was blocked by incubating the sections in a 1× TBS solution containing 5% normal donkey serum (Jackson ImmunoResearch Laboratories, #017000121), 0.1% Triton X-100 (Sigma-Aldrich; #X100) for 1 h at room temperature. Sections were incubated with goat anti-Iba1 (Abcam #ab5076; 1:500) and rabbit anti-Tmem119 (Abcam #Ab185333; 1:500) overnight at 4°C. After several washes with 1× TBS, sections were incubated for 2 h at room temperature with the following secondary antibodies: AlexaFluor-488 donkey anti-goat IgG (Molecular probes/Life Technologies #A11055; 1:1,000) and AlexaFluor-555 donkey anti-rabbit IgG (Molecular probes/Life Technologies #A31572; 1:1,000).

For cultured cells, after fixation (explained above) and several washes with 1× TBS, non-specific binding was blocked by incubating the sections in a solution of 5% normal donkey serum (Jackson ImmunoResearch Laboratories), 0.1% Triton X-100 (made in 1× TBS) for 1 h at room temperature. Cells were incubated overnight with the following primary antibodies: mouse anti-γH2AX (Phospho S139; Abcam #Ab26350; 1:500); rabbit anti-cGAS (D3O8O; Cell signaling technology #31659; 1:250); rabbit anti-phospho-STING (Ser365; Cell signaling technology #62912; 1:250). Cells were incubated for 1 h at room temperature with the appropriate secondary antibody. The following antibodies were used: AlexaFluor-488 donkey anti-rabbit IgG (Molecular probes/Life Technologies #A-21206; 1:1,000); AlexaFluor-555 donkey anti-rabbit IgG (Molecular probes/Life Technologies #A31572; 1:1,000); CF-555 donkey anti-mouse IgG (Biotium #20037; 1:1,000).

Hoechst 33342 (Molecular Probes/Life Technologies #H3570) was used as a nuclear counterstain. Slides were coverslipped using ProLong Gold anti-fade reagent (Molecular probes/Life Technologies; #P36930).

Microscopy and Cell quantification

All histological analyses were performed in the molecular layer (ML) and the *Cornu Ammonis* 1 (CA1) region of the hippocampus in sections containing the dorsal hippocampus spaced 300 μm apart (*i.e.* every 1:12 series). Analyses of total Ki67 positive ($Ki67^{+}$) cells, proliferating microglia ($Iba1^{+}/Ki67^{+}$) or Oligodendrocyte progenitors ($Olig2^{+}/Ki67^{+}$), parenchymal microglia ($Iba1^{+}/Tmem119^{high}$) and infiltrated macrophages ($Iba1^{+}/Tmem119^{negative}$ or $Iba1^{+}/Tmem119^{low}$) were performed using the LSM 700 Zeiss confocal scanning microscopy (Carl Zeiss, Germany), equipped with the Zen software (Black edition 2012, Carl Zeiss). Z-stack images were acquired in sequential scans performed at 1 μm section intervals using a 20× objective lens and 1 airy pinhole setting and analyzed using Zen Blue Lite software version 3.2 (Carl Zeiss). The fluorescent intensities of $Tmem119^{+}$ cells observed in the microglia of sham controls were considered $Tmem119^{high}$, and signals below those levels were considered $Tmem119^{low}$. The total numbers $Iba1^{+}$ cells over the time post-IR, were quantified using a bright field microscope (AxioImager M2; Carl Zeiss microscopy, Germany) equipped with the StereoInvestigator software (MicroBrightField Inc.); or in images were acquired using ZEISS Axio Scan.Z1 slide scanner (Carl Zeiss microscopy, Germany). In all quantifications, the total number of cells was the sum of all counted cells in all sections per animal multiplied by the series interval (*i.e.* 1:12). The cell density was determined by dividing the total number of quantified cells by counting volume.

Morphological analyses of parenchymal microglia ($Iba1^{+}/Tmem119^{high}$) and microglia-like cells ($Iba1^{+}/Tmem119^{negative\ or\ low}$) were performed on the Imaris software (Imaris V9.6).

Confocal z-stack images were processed for 3-D reconstruction, and individual Iba-1 positive cells were isolated using the surface tool. The filament tracer tool was then applied to every masked surface. The mean diameter of the processes, area coverage, and number of branching points were then analyzed.

For analysis of micronuclei and cGAS expression in SH or IR BV2 microglial cells, images were acquired using the LSM 700 laser scanning confocal microscope (Carl Zeiss, Germany) equipped with the Zen software (Black edition 2012, Carl Zeiss), using a 20× objective lens and 1× digital zoom. For analysis of phosph-STING, images were acquired using the ZEISS Axio Scan.Z1 slide scanner (Carl Zeiss microscopy, Germany). For each SH or IR condition, three coverslips were analyzed. Per coverslip, at least seven random fields were imaged covering the borders and the center of the coverslip. Image analysis was performed using the Zen Blue Lite software version 3.2 (Carl Zeiss). To analyze the percentage of cells with concomitant micronuclei and cGAS expression, at least 2,300 and 1,100 cells (Hoechst^{+}) from SH and IR cells were analyzed, respectively. A micronucleus is defined as a discrete Hoechst^{+} DNA aggregate apart from the primary nucleus of the cell. For analysis of phosph-STING expression, at least 1,200 and 700 cells from SH and IR cells were analyzed, respectively.

Protein extraction, ELISA and immunoblotting

For protein extraction from the hippocampal tissues, ice-cold protein extraction buffer (50 mM Tris-HCl; Sigma-Aldrich #T1503, 100 mM NaCl; Sigma-Aldrich, #S7653; 5 mM EDTA, Sigma-Aldrich #E5134 and 1 mM EGTA, Sigma-Aldrich #E3889) supplemented with protease inhibitor cocktail (Roche #11836170001) and phosphatase inhibitors (Roche #04906837001) were added to the frozen tissue and homogenized with a sonicator. Samples were then centrifuged for 10 min an 4°C at 10,000 × g and the supernatants were transferred

into 0.5 ml tubes and stored at -80°C. The total protein concentration was determined using the Pierce BCA protein assay kit (Thermo Fischer Scientific #23225), and absorbance was measured using FLUOstar Omega (BMG LABTECH, Germany) plate reader.

The levels of the chemokines in the hippocampal homogenates were measured using the following ELISA kits: mouse IP-10 (CXCL10) ELISA kit (Abcam #ab214563), mouse MCP5 (CCL12) ELISA kit (Abcam #ab100723) and mouse/rat CCL2/JE/MCP-1 quantikine ELISA kit (R&D Systems #MJE00). The assays were performed following the manufacturer's instructions. For BV2 cells, after media aspiration and gentle washing with 1× PBS, a 2.5× loading buffer (Tris HCl 62 mM; 2 % Sodium dodecyl sulfate; 10 % Glycerol; 5 % β-mercaptoethanol; 0.02 % Bromphenol Blue) was added, and cells were collected. Cells were then sonicated, and the attained protein extracts were processed for western blot. Proteins were detected using the following antibodies: rabbit anti-phospho-TBK1/NAK (Ser172) (D52C2); Cell Signaling #5483; 1:1,000); mouse anti-β-actin (Sigma-Aldrich #A2228; 1:2,000). Membranes were visualized using the Odyssey CLx LI-COR equipped with the Image Studio software. Protein band densitometry was done using the ImageJ software. The target to housekeeping protein (β-actin) expression ratio was used to quantify protein expression and sham controls were set as 1.

Assessment of gamma oscillations

Mice were sacrificed 2 weeks, 6 week, 6 months or 1 year post-IR. Animals were anesthetized with isoflurane and decapitated. Brains were quickly dissected and placed in ice-cold artificial cerebrospinal fluid (ACSF) modified for dissection containing (in mM): 80 NaCl, 24 $NaHCO_3$, 25 glucose, 1.25 NaH_2PO_4, 1 ascorbic acid, 3 Na-pyruvate, 2.5 KCl, 4 $MgCl_2$, 0.5 $CaCl_2$, 75 sucrose (Sigma-Aldrich) and bubbled with carbogen (95% O_2 and 5% CO_2). Horizontal hippocampal sections 3,500 µm thick were prepared from the two

hemispheres using a Leica VT1200S vibratome (Leica Microsystems). Slices were immediately placed into an interface holding chamber containing standard ACSF (in mM): 124 NaCl, 30 $NaHCO_3$, 10 glucose, 1.25 NaH_2PO_4, 3.5 KCl, 1.5 $MgCl_2$, 1.5 $CaCl_2$ (Sigma-Aldrich) continuously supplied with humidified carbogen gas (95% O_2 and 5% CO_2). The chamber was held at 34ºC during the slicing process and subsequently allowed to cool down to room temperature (~22ºC) for at least 1 h in order to let the slices recover.

Hippocampal gamma oscillations experiments were performed in a submerged-type recording chamber as described previously [53]. Local field potentials (LFP) were recorded using microelectrodes filled with standard ACSF placed in the CA3 *stratum pyramidale* and elicited by adding kainic acid (100 nM; Tocris Bioscience) to the extracellular bath.

Oscillation power spectra, fast fourier transformations were obtained from 60 s of LFP recording (segment length 8192 points) using the Axograph X software (Kagi, Berkeley, CA, USA). Frequency variance data was obtained from the power spectra described above using Axograph X. Gamma power was calculated by integrating the power spectral density from 20 to 80 Hz using Clampfit 11.2.

Human tissue

The clinical samples used in this study were provided by the Swedish Children's Tumor Bank (Barntumörbanken; ethical application nr. 2021-02333). The cancer-free hippocampal tissue was obtained from the autopsied brain tissue of a 12-year-old patient with Group 4 medulloblastoma collected 5 years post-radiotherapy. The tumor-bearing tissue was collected at surgical reresection of an ependymoma from a 4-year-old patient upon a tumor relapse 1 year and 10 months after the initial surgery. The healthy human hippocampal tissue used as a control for the immunofluorescence staining was purchased from Clinisciences (Biochain; #T2234052). This tissue was donated by a healthy 54-year-old male. BioChain's tissue products are based on the sample repository network established following the approved ethical standards and procedures. All tissues were paraffin-embedded and cut into 5 μm-thick sections.

Statistical analysis

Statistical analyses were performed using GraphPad Prism (GraphPad, Inc., San Diego, CA, USA). Data were presented as mean ± SEM. The unpaired student's t-test was used to compare SH and IR animals at each time point, aiming to eliminate the effect of animal age. Comparisons of multiple variants per time point were performed using a two-way ANOVA with Bonferroni's *posthoc* for multiple comparisons. Significance was considered when $p < 0.05$. The statistical analyses, number of animals and *in vitro* experiments applied were noted in each figure legend. For the bulk RNA-seq data analyses, Qlucore Omics Explorer 3.2 software (Qlucore, Lund, Sweden) was used. The GSEAP reranked tool was used for the GSEA analysis, while for single-cell RNA-seq data analyses, both R software (version 3.0.0) and the Seurat package (version 4.0.0) were used.

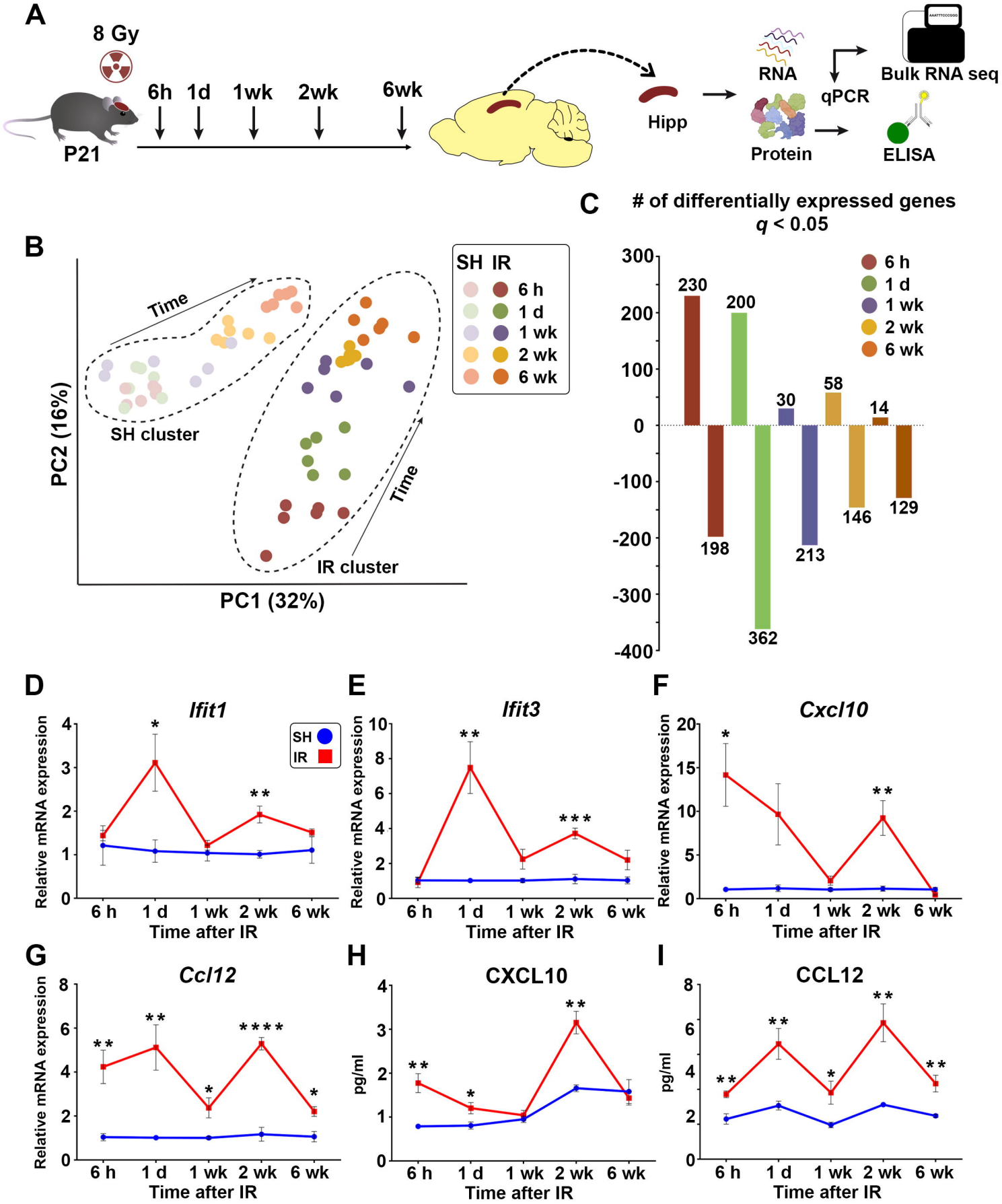
A
8 Gy
P21
6h
1d
1wk
2wk
6wk
Hipp
RNA
Protein
qPCR
Bulk RNA seq
ELISA
B
SH IR
6 h
1 d
1 wk
2 wk
6 wk
Time
SH cluster
IR cluster
PC2 (16%)
PC1 (32%)
C
# of differentially expressed genes
q < 0.05
230
198
200
362
30
213
58
146
14
129
D
Ifit1
E
Ifit3
F
Cxcl10
G
Ccl12
H
CXCL10
I
CCL12
SH
IR
Relative mRNA expression
pg/ml
Time after IR

Figure 1

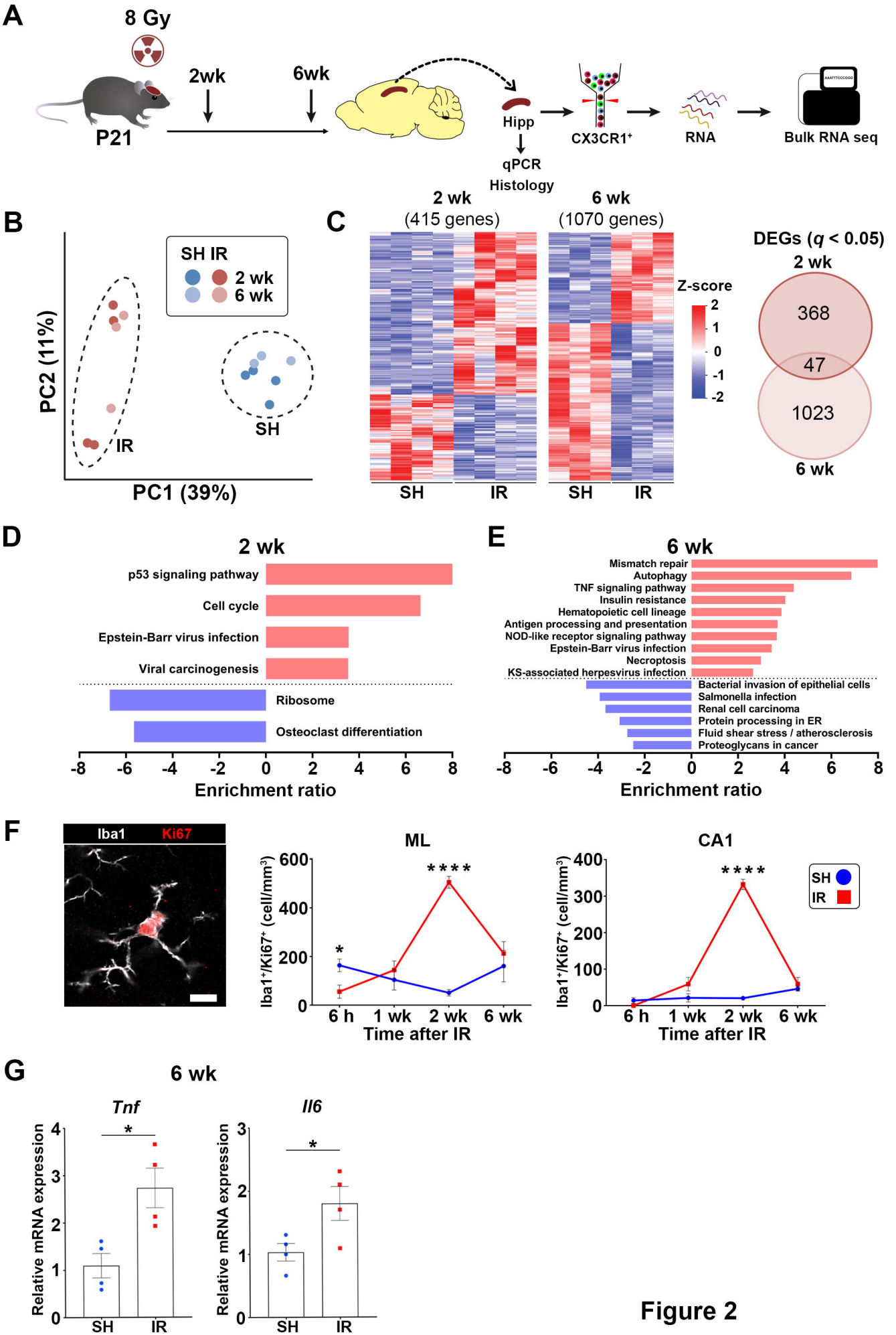
A
8 Gy
P21
2wk
6wk
Hipp
qPCR
Histology
CX3CR1+
RNA
Bulk RNA seq
B
SH IR
2 wk
6 wk
PC2 (11%)
PC1 (39%)
IR
SH
C
2 wk
(415 genes)
6 wk
(1070 genes)
Z-score
SH
IR
DEGs (q < 0.05)
2 wk
368
47
1023
6 wk
D
2 wk
p53 signaling pathway
Cell cycle
Epstein-Barr virus infection
Viral carcinogenesis
Ribosome
Osteoclast differentiation
Enrichment ratio
E
6 wk
Mismatch repair
Autophagy
TNF signaling pathway
Insulin resistance
Hematopoietic cell lineage
Antigen processing and presentation
NOD-like receptor signaling pathway
Epstein-Barr virus infection
Necroptosis
KS-associated herpesvirus infection
Bacterial invasion of epithelial cells
Salmonella infection
Renal cell carcinoma
Protein processing in ER
Fluid shear stress / atherosclerosis
Proteoglycans in cancer
Enrichment ratio
F
Iba1
Ki67
ML
CA1
Iba1+/Ki67+ (cell/mm3)
Time after IR
6 h
1 wk
2 wk
6 wk
SH
IR
G
6 wk
Tnf
Il6
Relative mRNA expression
SH
IR

Figure 2

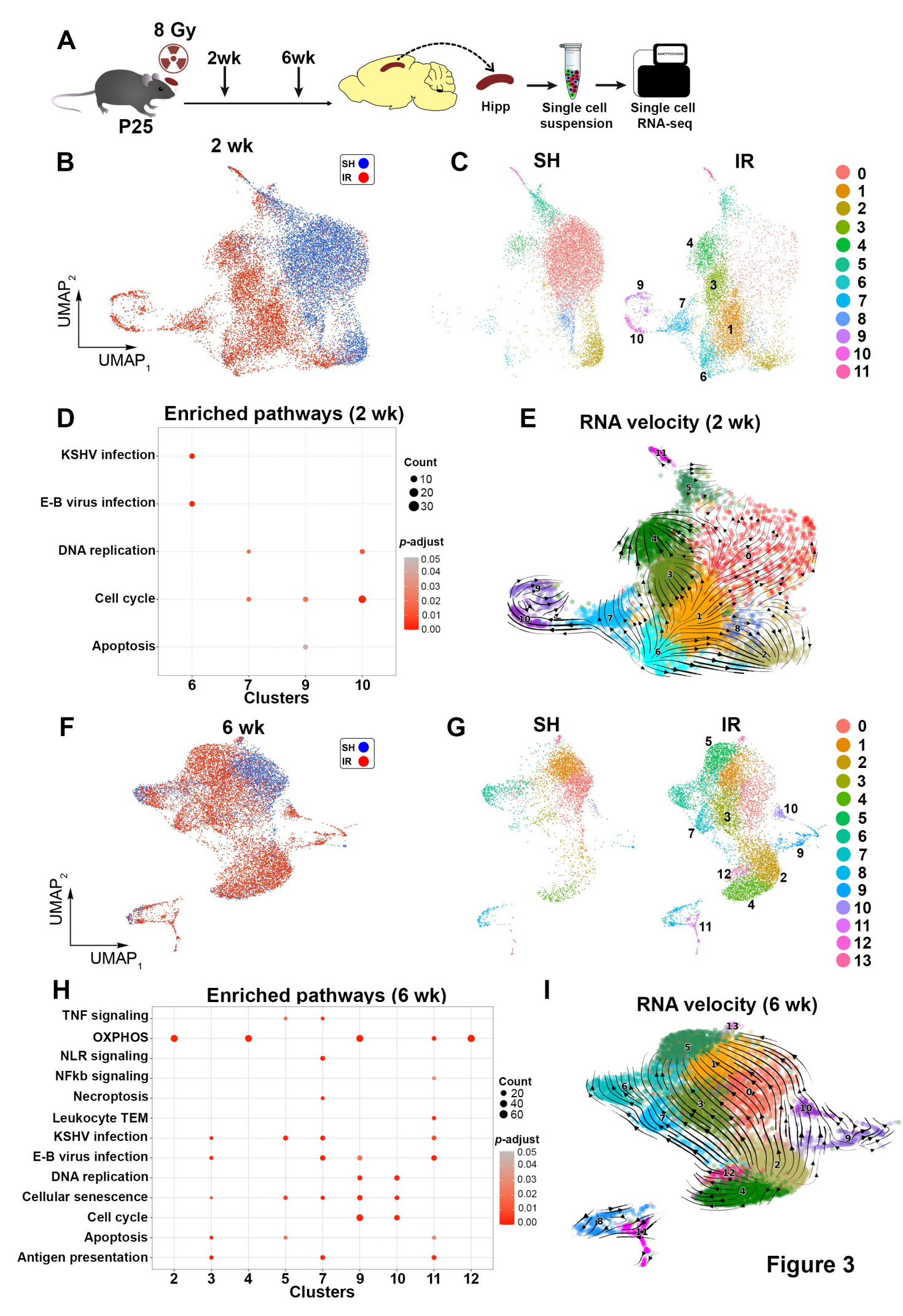
A
8 Gy
2wk
6wk
P25
Hipp
Single cell suspension
Single cell RNA-seq
B
2 wk
SH
IR
UMAP2
UMAP1
C
SH
IR
0
1
2
3
4
5
6
7
8
9
10
11
D
Enriched pathways (2 wk)
KSHV infection
E-B virus infection
DNA replication
Cell cycle
Apoptosis
Count
10
20
30
p-adjust
0.05
0.04
0.03
0.02
0.01
0.00
6
7
9
10
Clusters
E
RNA velocity (2 wk)
F
6 wk
SH
IR
UMAP2
UMAP1
G
SH
IR
0
1
2
3
4
5
6
7
8
9
10
11
12
13
H
Enriched pathways (6 wk)
TNF signaling
OXPHOS
NLR signaling
NFkb signaling
Necroptosis
Leukocyte TEM
KSHV infection
E-B virus infection
DNA replication
Cellular senescence
Cell cycle
Apoptosis
Antigen presentation
Count
20
40
60
p-adjust
0.05
0.04
0.03
0.02
0.01
0.00
2
3
4
5
7
9
10
11
12
Clusters
I
RNA velocity (6 wk)
Figure 3

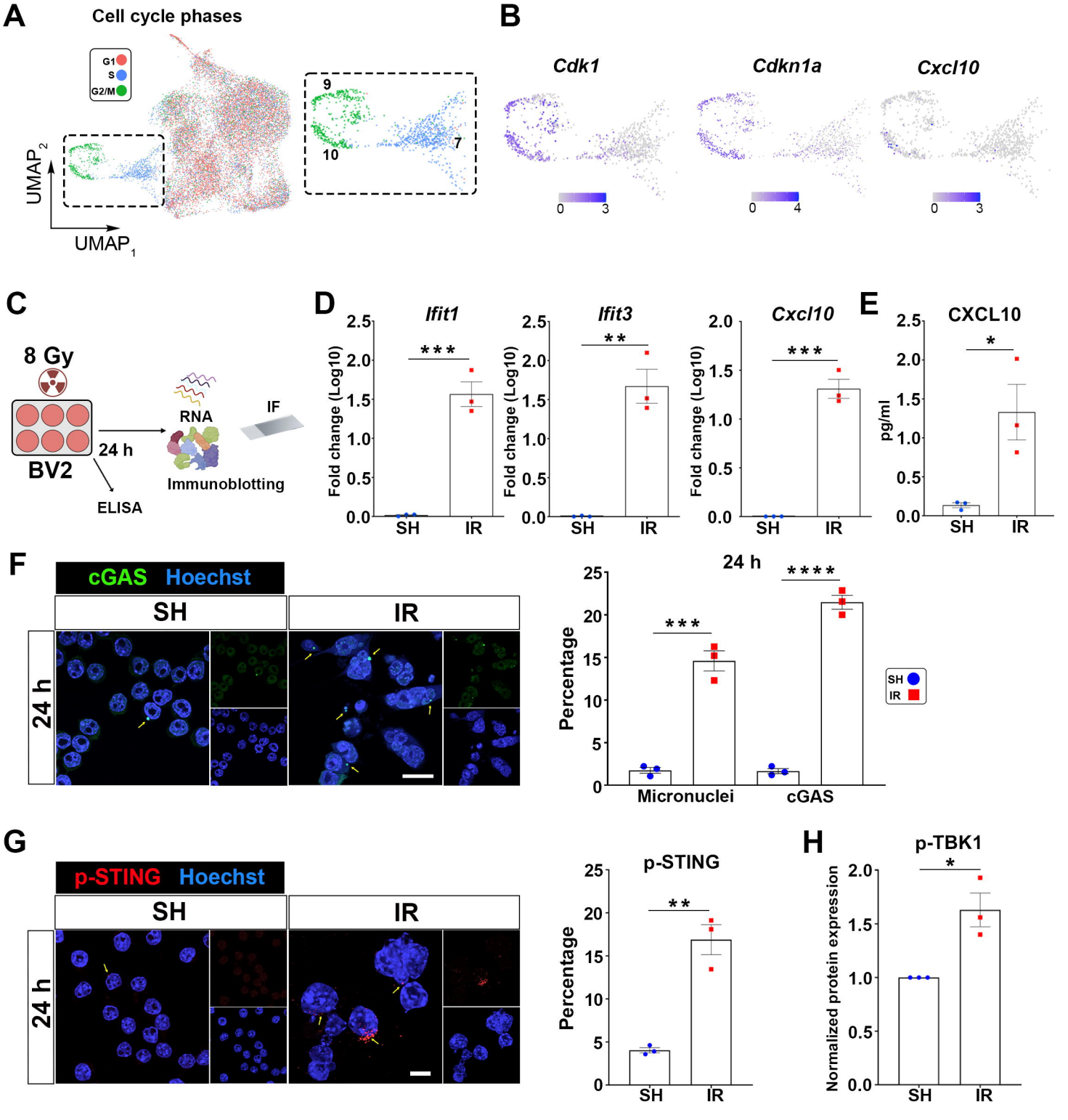
A
Cell cycle phases
G1
S
G2/M
9
10
7
UMAP2
UMAP1
B
Cdk1
Cdkn1a
Cxcl10
0 3
0 4
0 3
C
8 Gy
BV2
24 h
RNA
IF
Immunoblotting
ELISA
D
Ifit1
Ifit3
Cxcl10
Fold change (Log10)
SH
IR
E
CXCL10
pg/ml
F
cGAS Hoechst
SH
IR
24 h
Percentage
Micronuclei
cGAS
G
p-STING Hoechst
p-STING
H
p-TBK1
Normalized protein expression

Figure 4

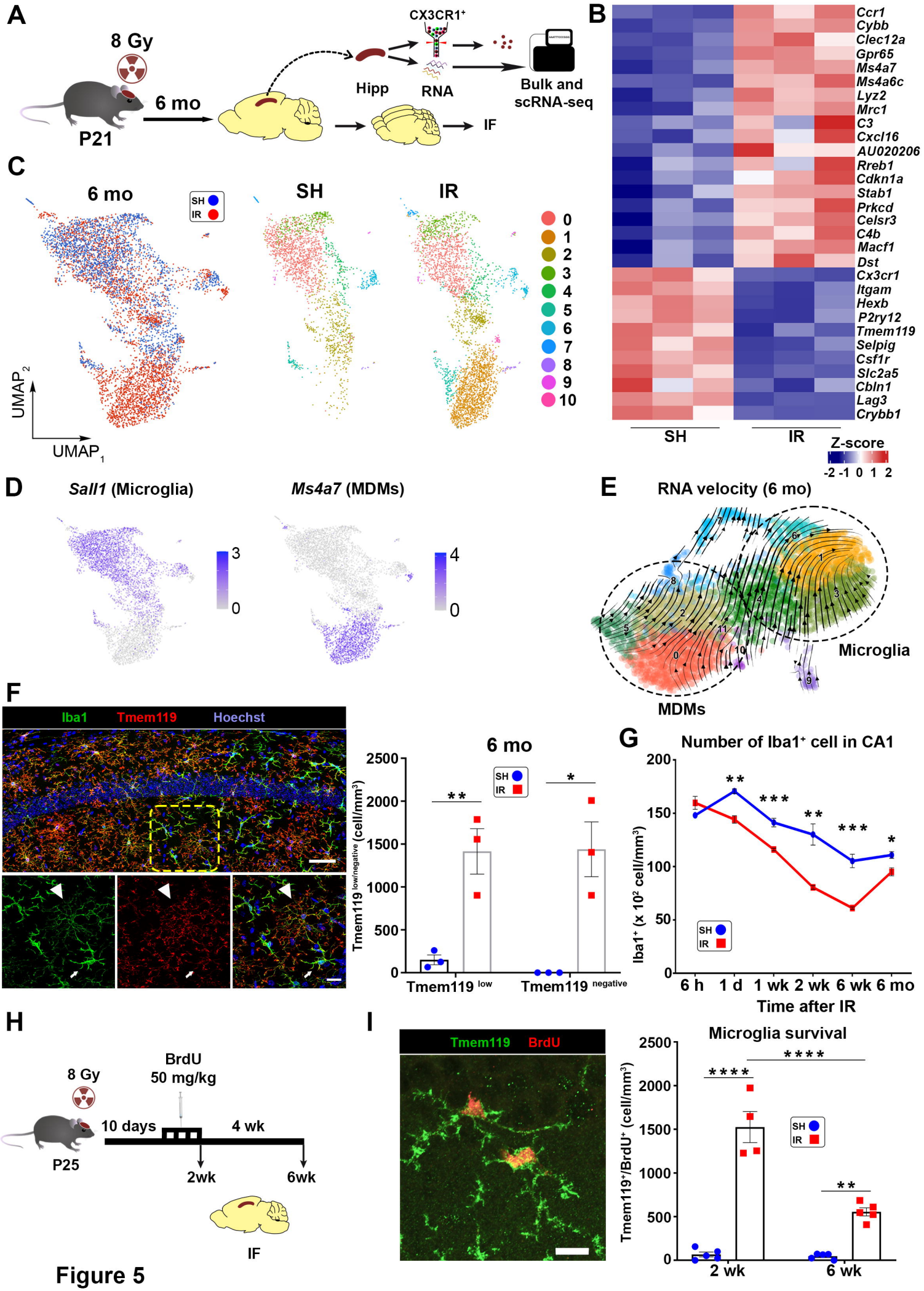
A
8 Gy
6 mo
P21
CX3CR1+
Hipp
RNA
Bulk and scRNA-seq
IF
B
Ccr1
Cybb
Clec12a
Gpr65
Ms4a7
Ms4a6c
Lyz2
Mrc1
C3
Cxcl16
AU020206
Rreb1
Cdkn1a
Stab1
Prkcd
Celsr3
C4b
Macf1
Dst
Cx3cr1
Itgam
Hexb
P2ry12
Tmem119
Selpig
Csf1r
Slc2a5
Cbln1
Lag3
Crybb1
SH
IR
Z-score
-2 -1 0 1 2
C
6 mo
SH
IR
UMAP2
UMAP1
0
1
2
3
4
5
6
7
8
9
10
D
Sall1 (Microglia)
Ms4a7 (MDMs)
3
0
4
0
E
RNA velocity (6 mo)
Microglia
MDMs
F
Iba1
Tmem119
Hoechst
6 mo
Tmem119 low/negative (cell/mm3)
Tmem119 low
Tmem119 negative
G
Number of Iba1+ cell in CA1
Iba1+ (x 10² cell/mm³)
6 h
1 d
1 wk
2 wk
6 wk
6 mo
Time after IR
H
8 Gy
BrdU
50 mg/kg
P25
10 days
4 wk
2wk
6wk
IF
I
Tmem119
BrdU
Microglia survival
Tmem119+/BrdU+ (cell/mm3)
2 wk
6 wk

Figure 5

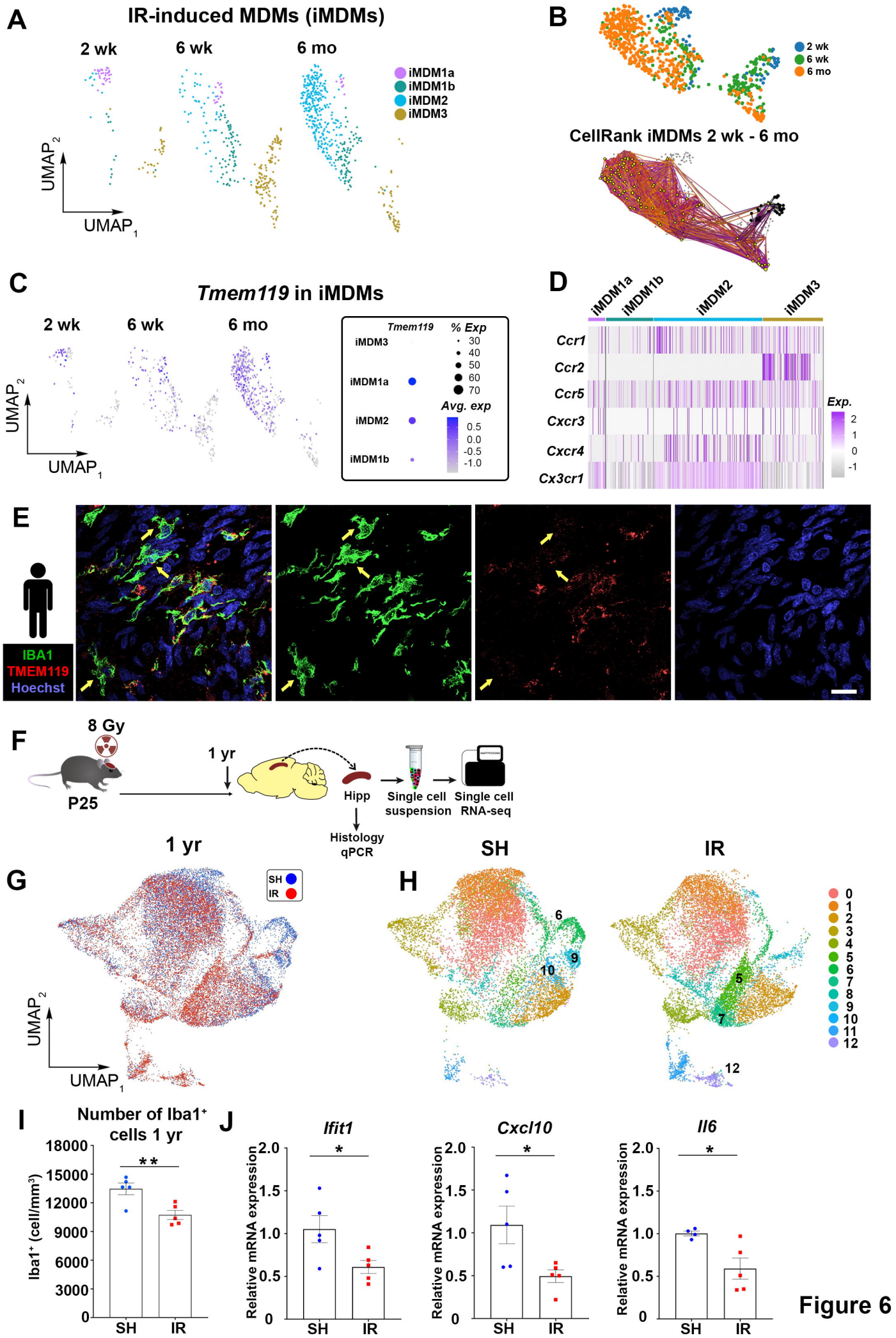
A
IR-induced MDMs (iMDMs)
2 wk
6 wk
6 mo
iMDM1a
iMDM1b
iMDM2
iMDM3
UMAP2
UMAP1
B
2 wk
6 wk
6 mo
CellRank iMDMs 2 wk - 6 mo
C
Tmem119 in iMDMs
2 wk
6 wk
6 mo
Tmem119
% Exp
30
40
50
60
70
Avg. exp
0.5
0.0
-0.5
-1.0
iMDM3
iMDM1a
iMDM2
iMDM1b
D
iMDM1a
iMDM1b
iMDM2
iMDM3
Ccr1
Ccr2
Ccr5
Cxcr3
Cxcr4
Cx3cr1
Exp.
2
1
0
-1
E
IBA1
TMEM119
Hoechst
F
8 Gy
P25
1 yr
Hipp
Single cell suspension
Single cell RNA-seq
Histology qPCR
1 yr
SH
IR
G
SH
IR
H
6
9
10
5
7
12
0
1
2
3
4
5
6
7
8
9
10
11
12
I
Number of Iba1+ cells 1 yr
Iba1+ (cell/mm3)
18000
15000
12000
9000
6000
3000
0
**
SH
IR
J
Ifit1
Cxcl10
Il6
Relative mRNA expression
2.0
1.5
1.0
0.5
0
*
SH
IR

Figure 6

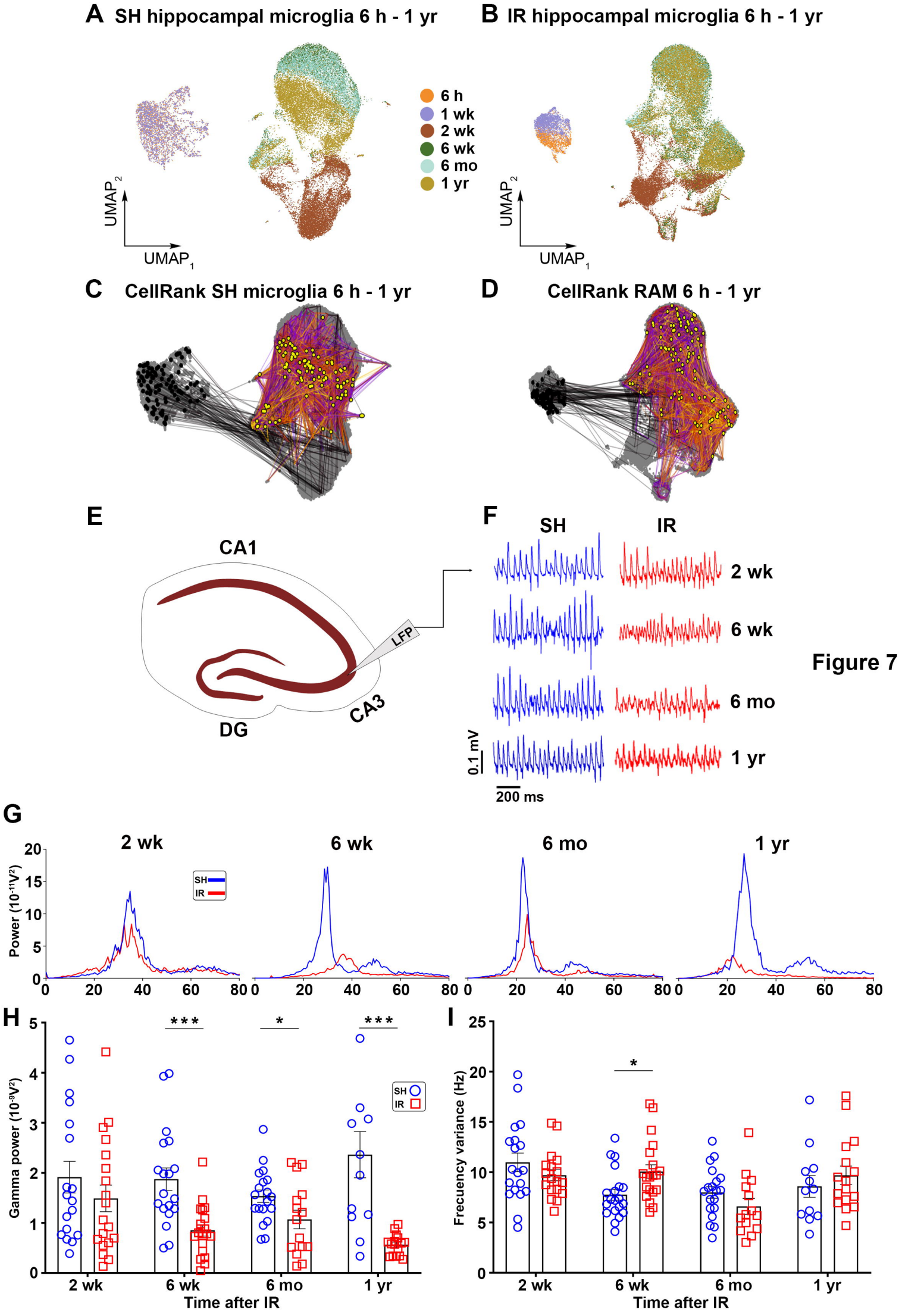
A SH hippocampal microglia 6 h - 1 yr
B IR hippocampal microglia 6 h - 1 yr
6 h
1 wk
2 wk
6 wk
6 mo
1 yr
UMAP2
UMAP1
C CellRank SH microglia 6 h - 1 yr
D CellRank RAM 6 h - 1 yr
E
CA1
LFP
CA3
DG
F
SH
IR
2 wk
6 wk
6 mo
1 yr
0.1 mV
200 ms
G
2 wk
6 wk
6 mo
1 yr
Power (10-11V2)
SH
IR
H
Gamma power (10-9V2)
***
*
***
SH
IR
2 wk
6 wk
6 mo
1 yr
Time after IR
I
Frecuency variance (Hz)
*
2 wk
6 wk
6 mo
1 yr
Time after IR

Figure 7

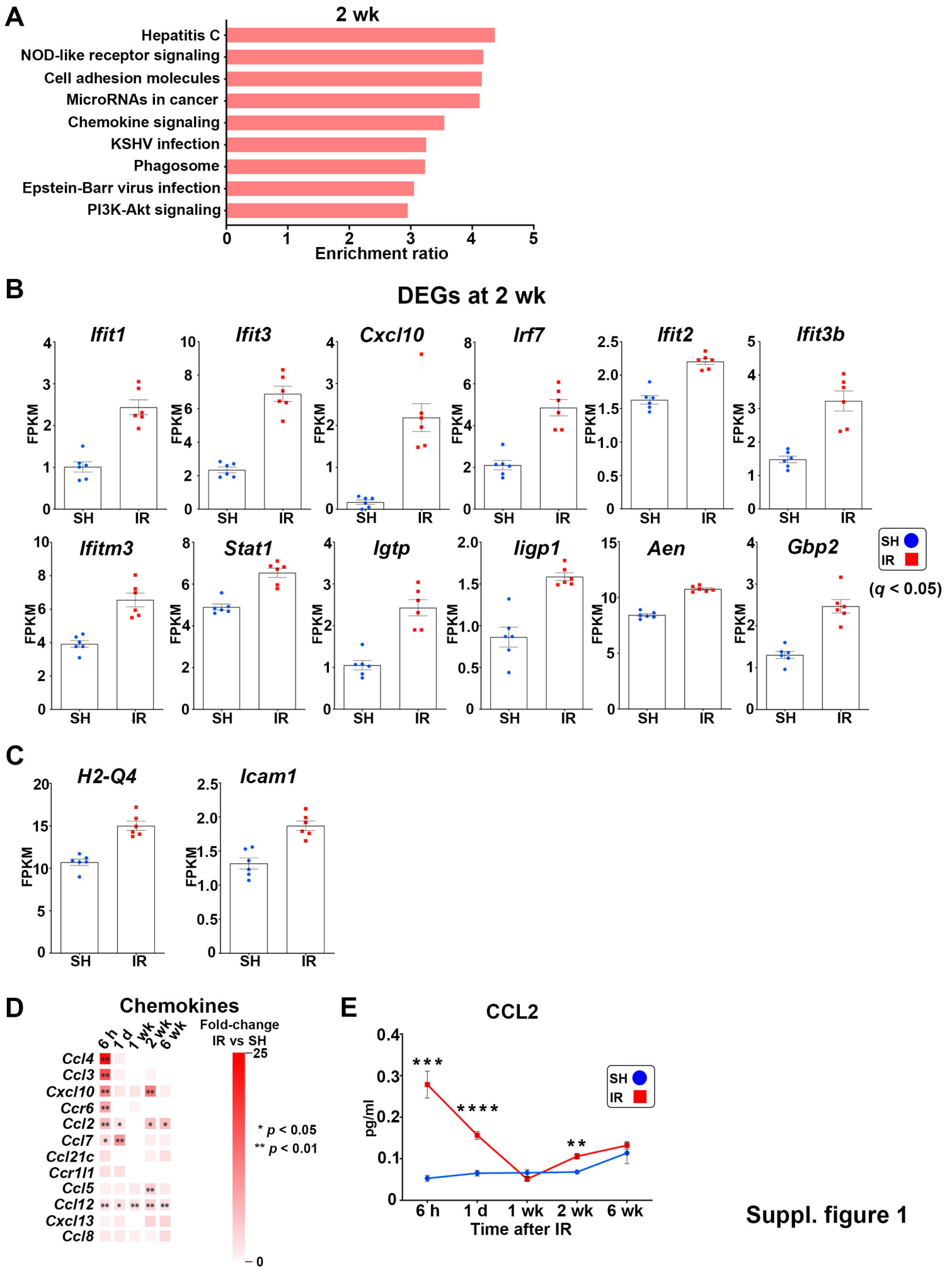
A
2 wk
Hepatitis C
NOD-like receptor signaling
Cell adhesion molecules
MicroRNAs in cancer
Chemokine signaling
KSHV infection
Phagosome
Epstein-Barr virus infection
PI3K-Akt signaling
0 1 2 3 4 5
Enrichment ratio
B
DEGs at 2 wk
Ifit1
Ifit3
Cxcl10
Irf7
Ifit2
Ifit3b
Ifitm3
Stat1
Igtp
Iigp1
Aen
Gbp2
FPKM
SH
IR
(q < 0.05)
C
H2-Q4
Icam1
D
Chemokines
6 h
1 d
1 wk
2 wk
6 wk
Fold-change
IR vs SH
Ccl4
Ccl3
Cxcl10
Ccr6
Ccl2
Ccl7
Ccl21c
Ccr1l1
Ccl5
Ccl12
Cxcl13
Ccl8
* p < 0.05
** p < 0.01
E
CCL2
pg/ml
Time after IR
Suppl. figure 1

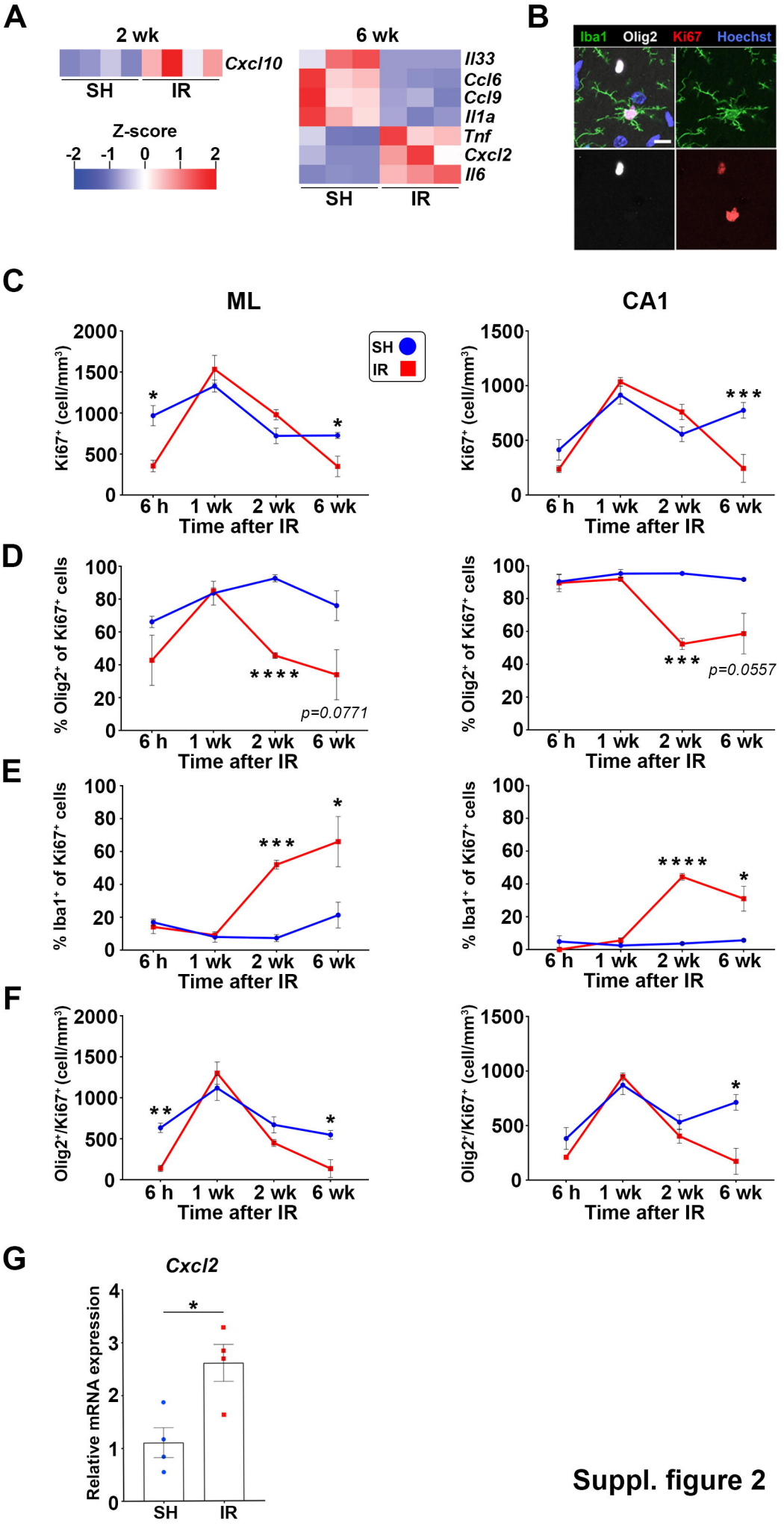

Suppl. figure 2

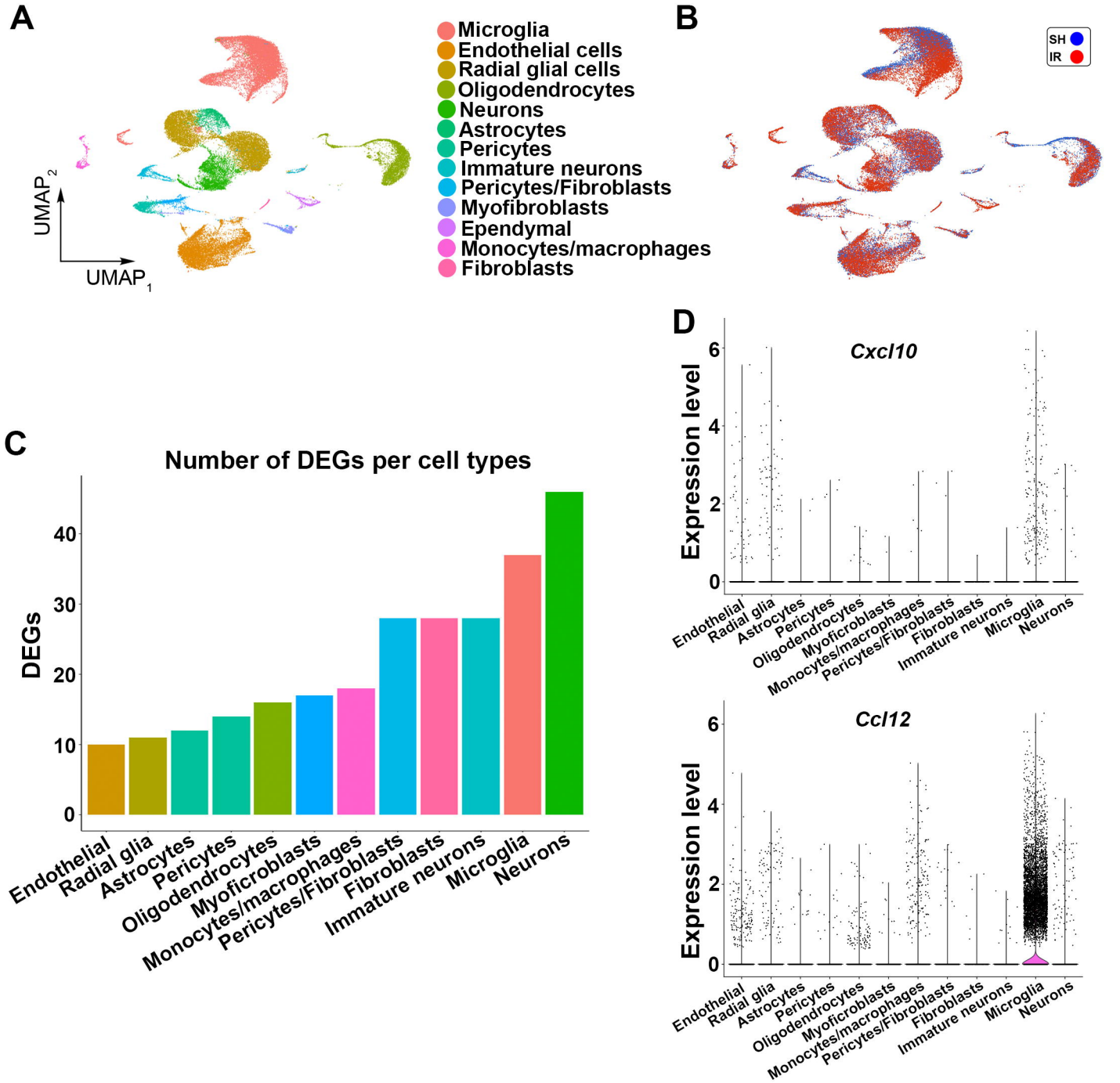

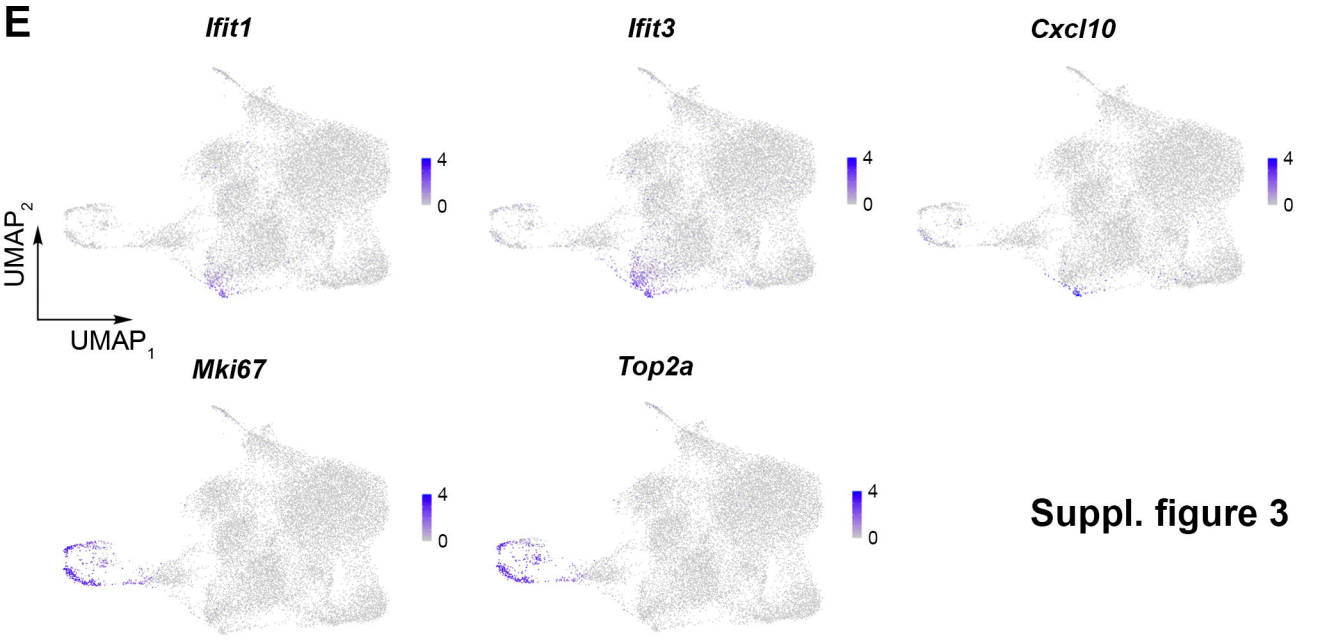

Suppl. figure 3

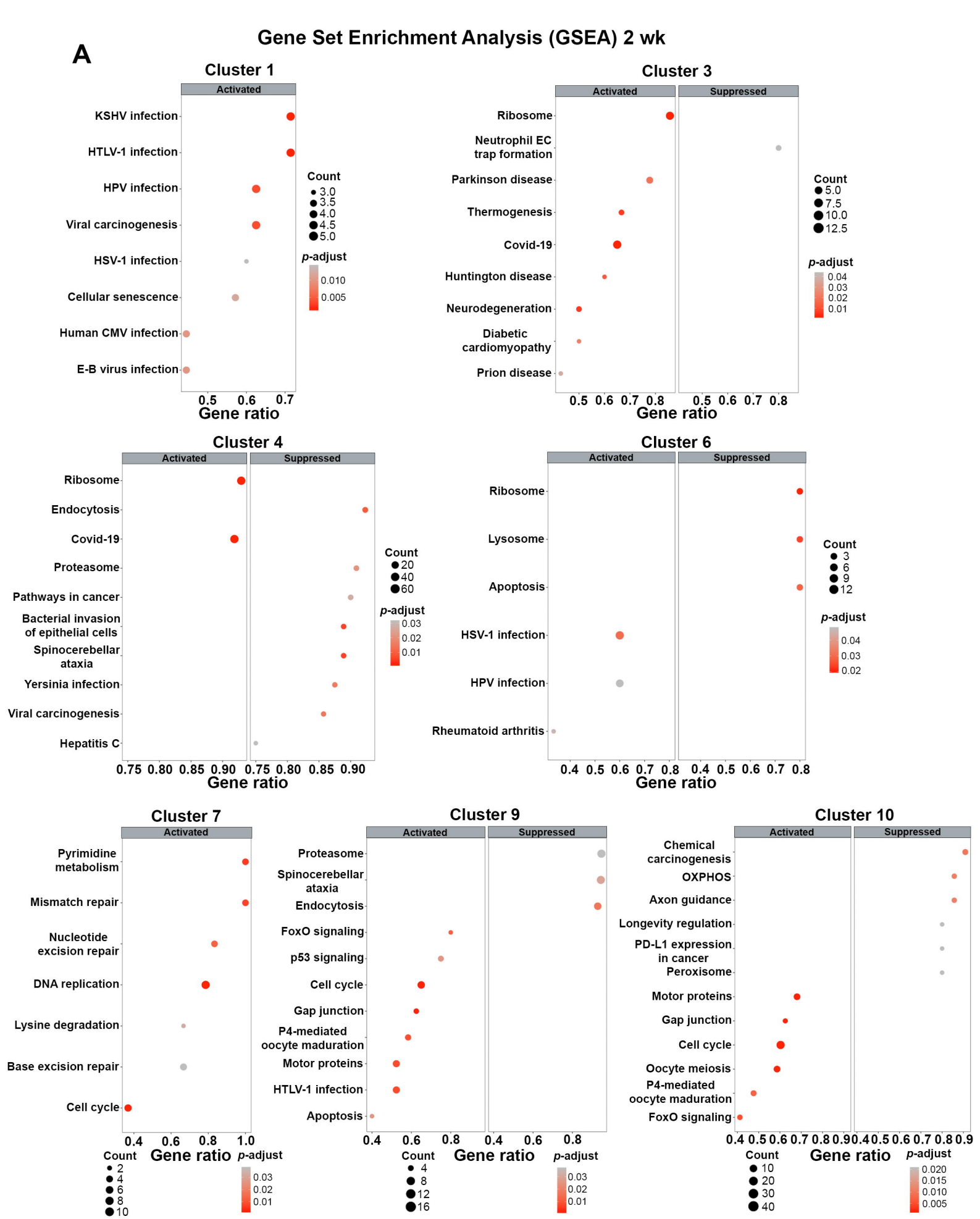

Suppl. figure 4

Gene Set Enrichment Analysis (GSEA) 6 wk

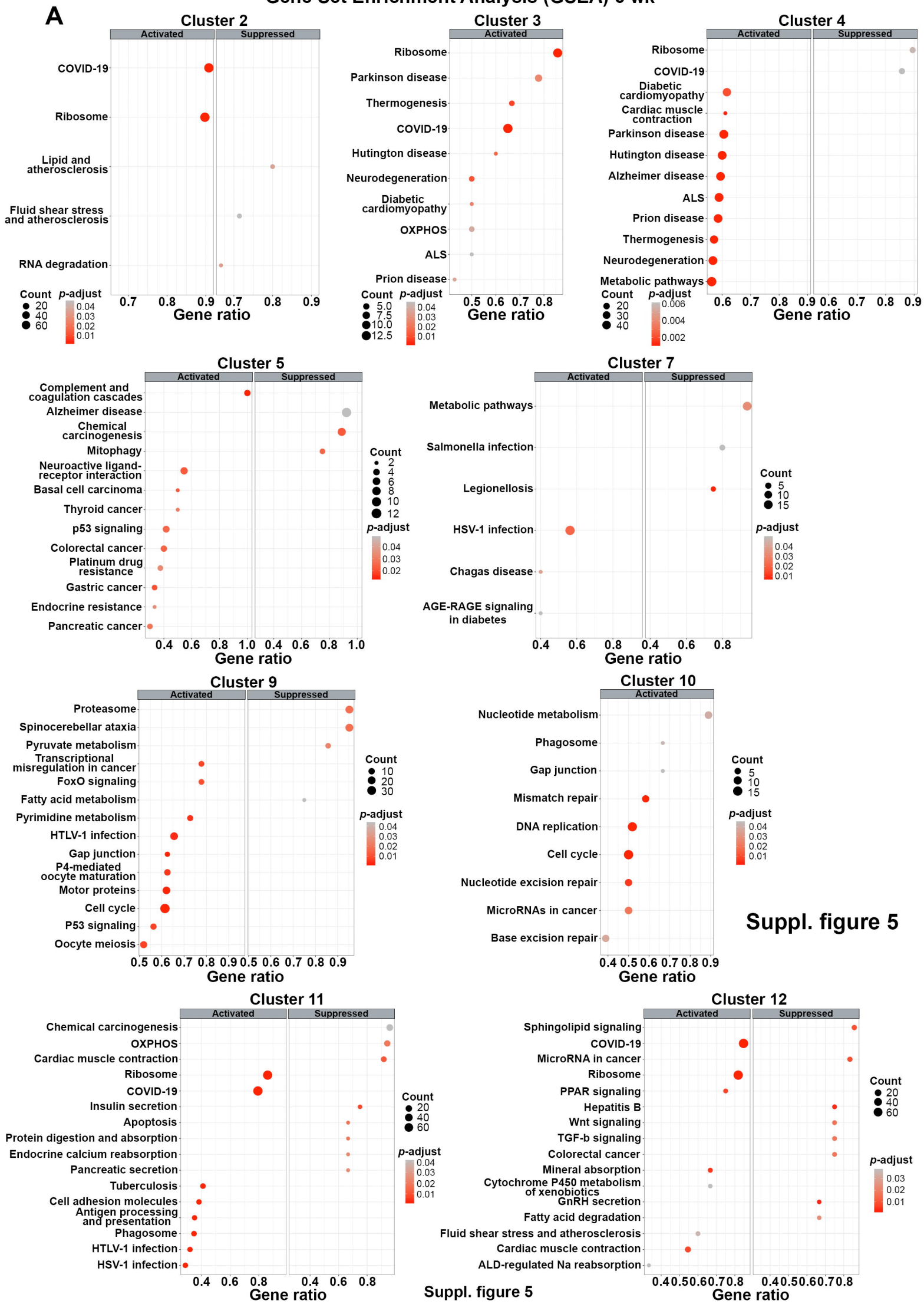

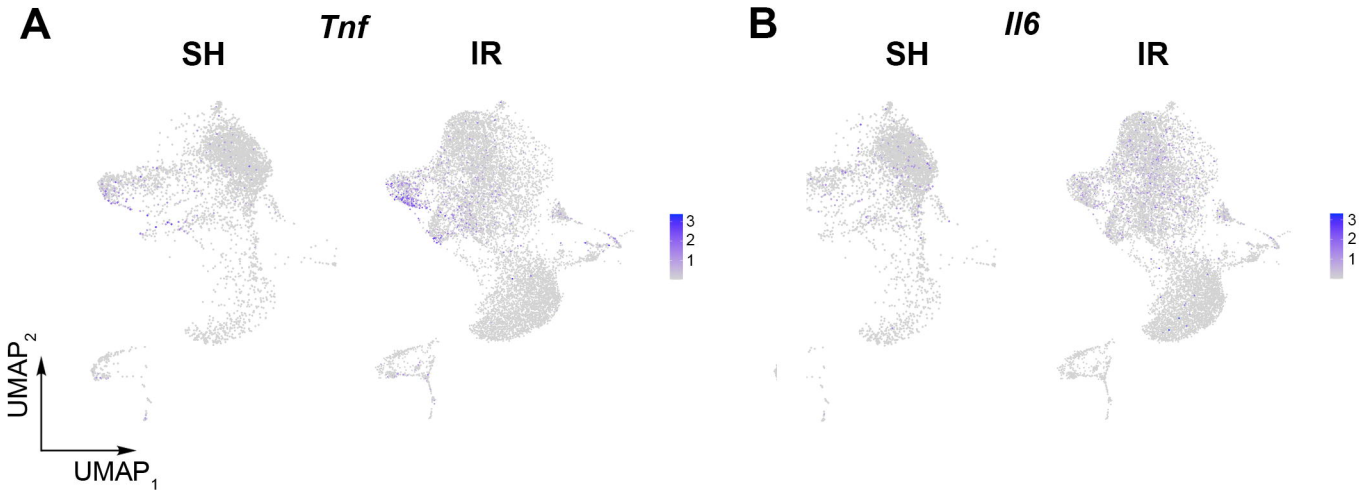

Suppl. figure 6

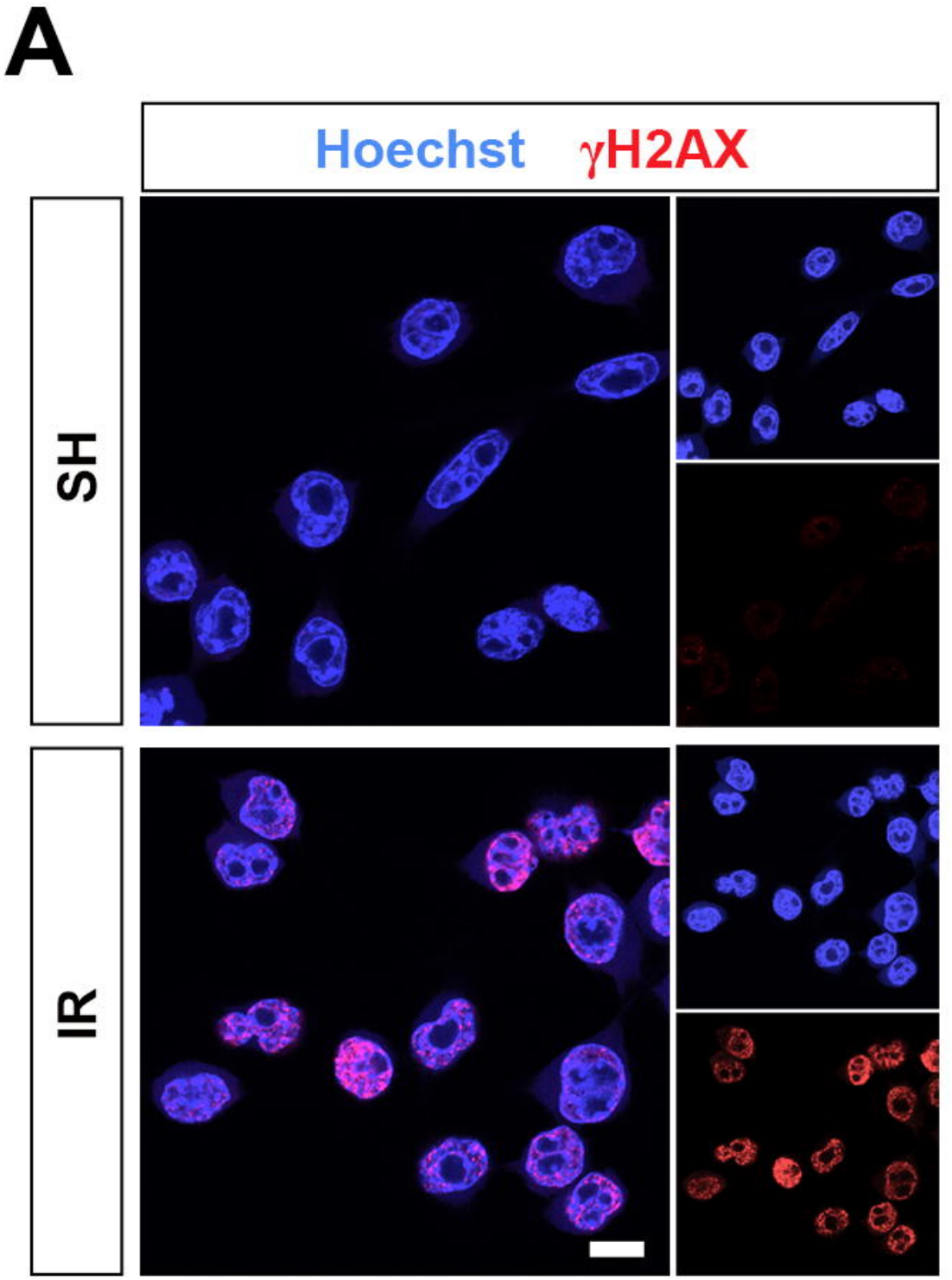

Suppl. figure 7

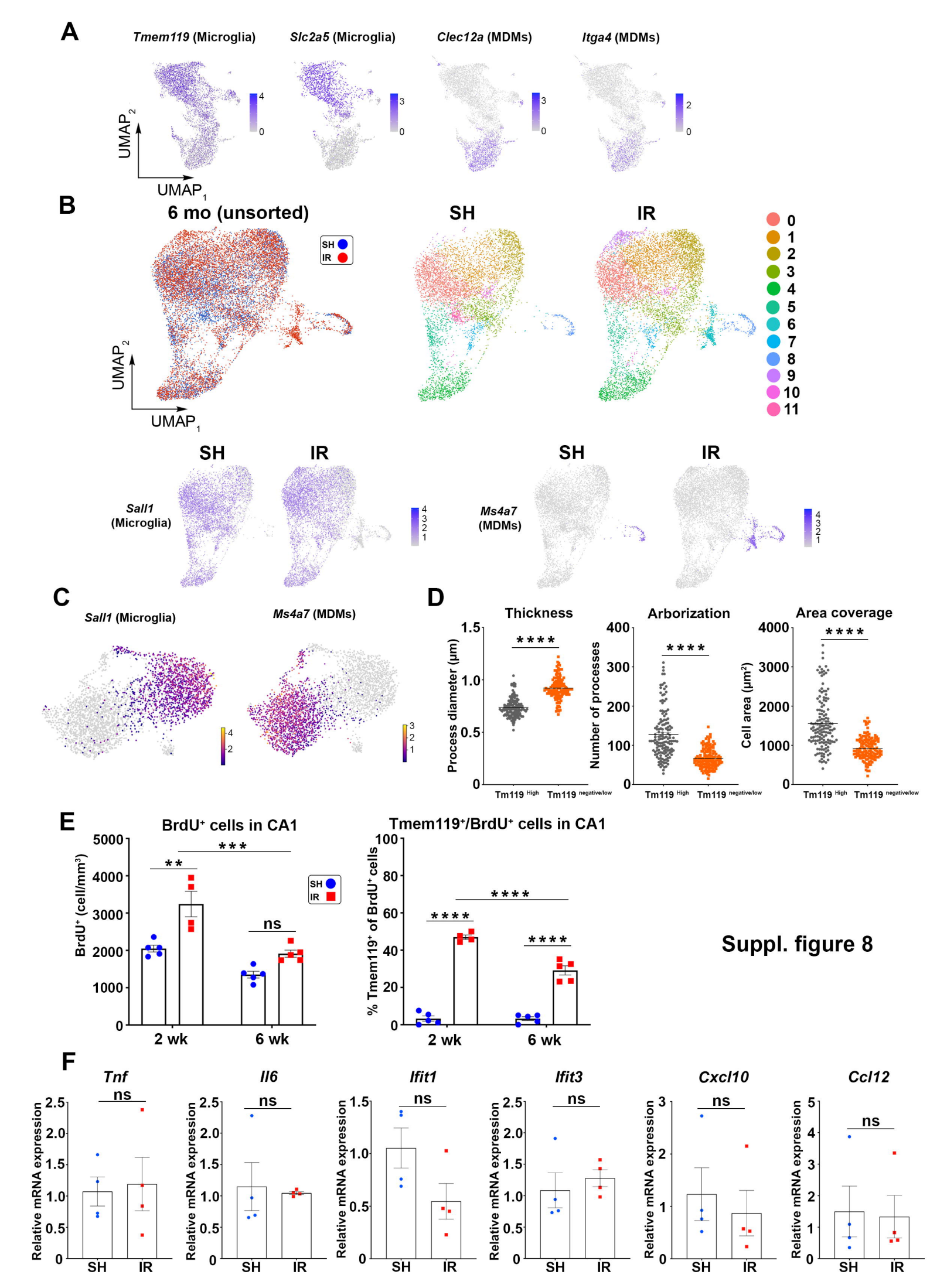
A
Tmem119 (Microglia)
Slc2a5 (Microglia)
Clec12a (MDMs)
Itga4 (MDMs)
UMAP2
UMAP1
B
6 mo (unsorted)
SH
IR
0
1
2
3
4
5
6
7
8
9
10
11
Sall1 (Microglia)
Ms4a7 (MDMs)
C
D
Thickness
Arborization
Area coverage
Process diameter (µm)
Number of processes
Cell area (µm²)
Tm119 High
Tm119 negative/low
E
BrdU⁺ cells in CA1
Tmem119⁺/BrdU⁺ cells in CA1
BrdU⁺ (cell/mm³)
% Tmem119⁺ of BrdU⁺ cells
2 wk
6 wk
ns
Suppl. figure 8
F
Tnf
Il6
Ifit1
Ifit3
Cxcl10
Ccl12
Relative mRNA expression

Border-associated macrophages and iMDMs

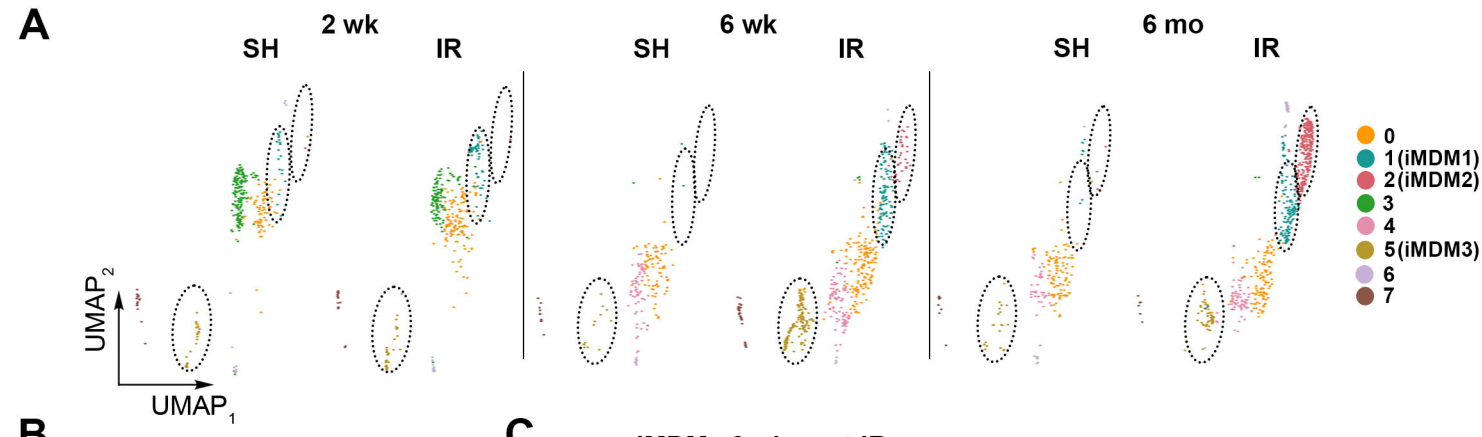

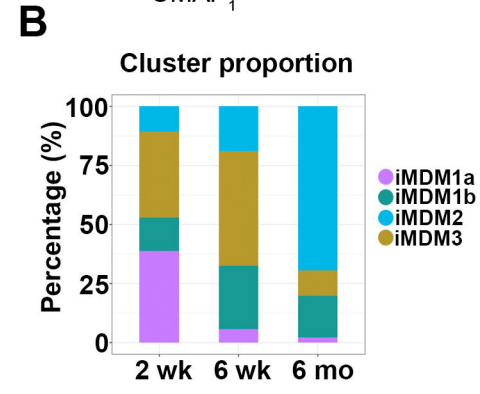

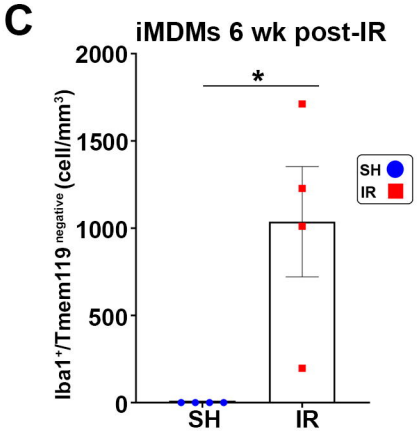

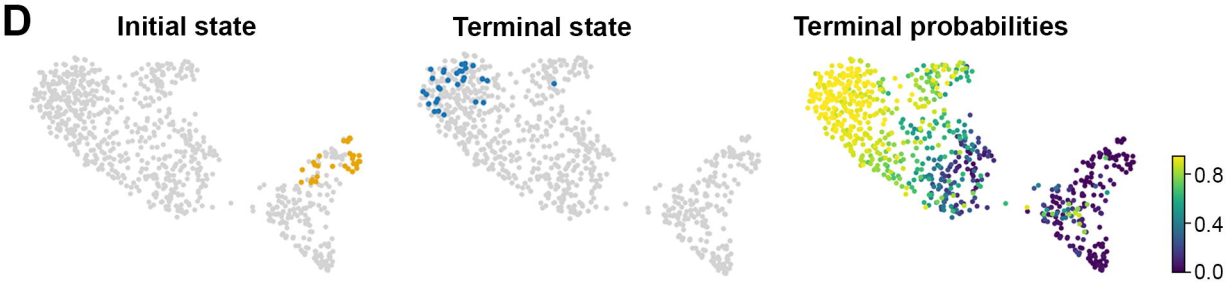

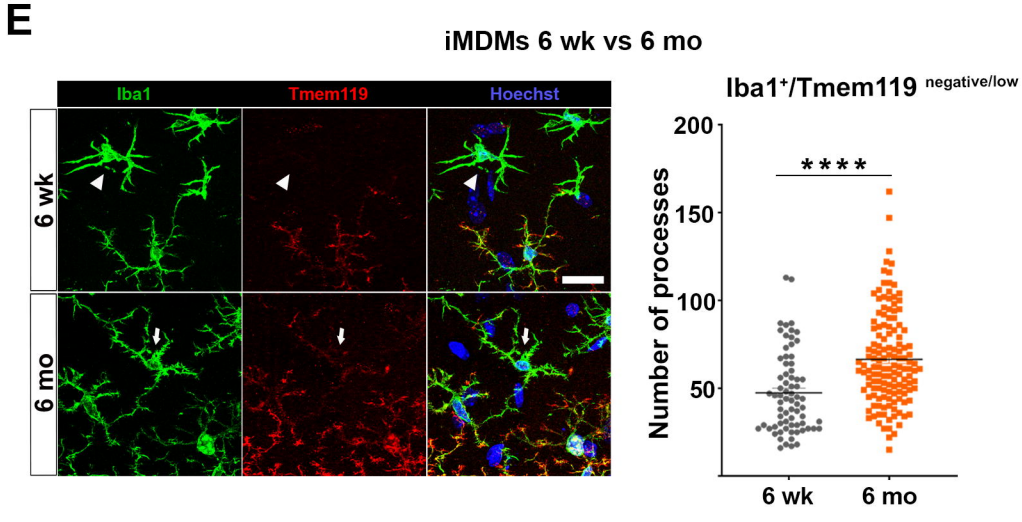

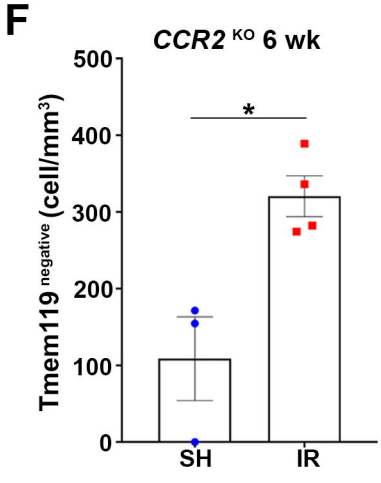

Suppl. figure 9

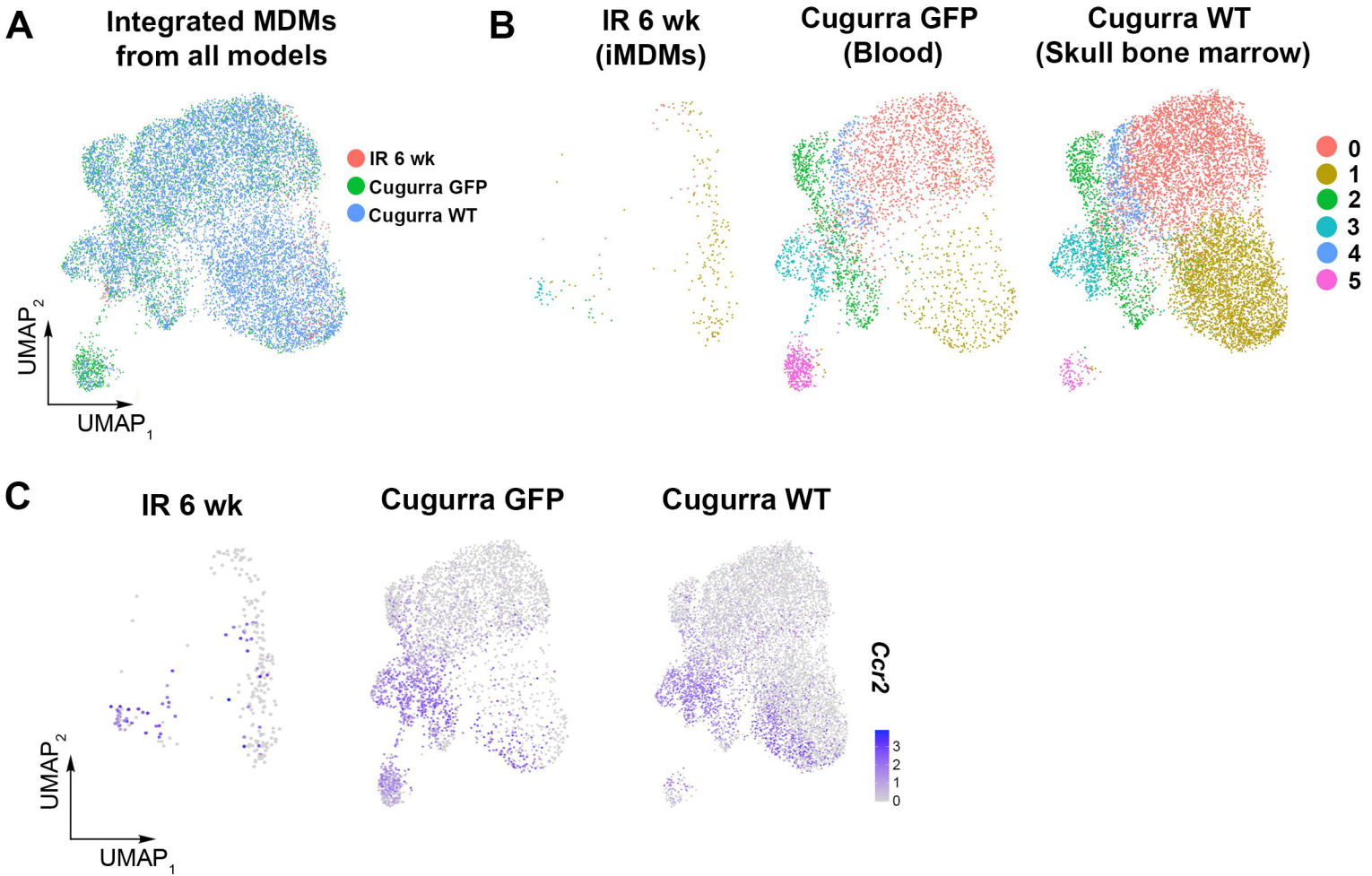

Suppl. figure 10

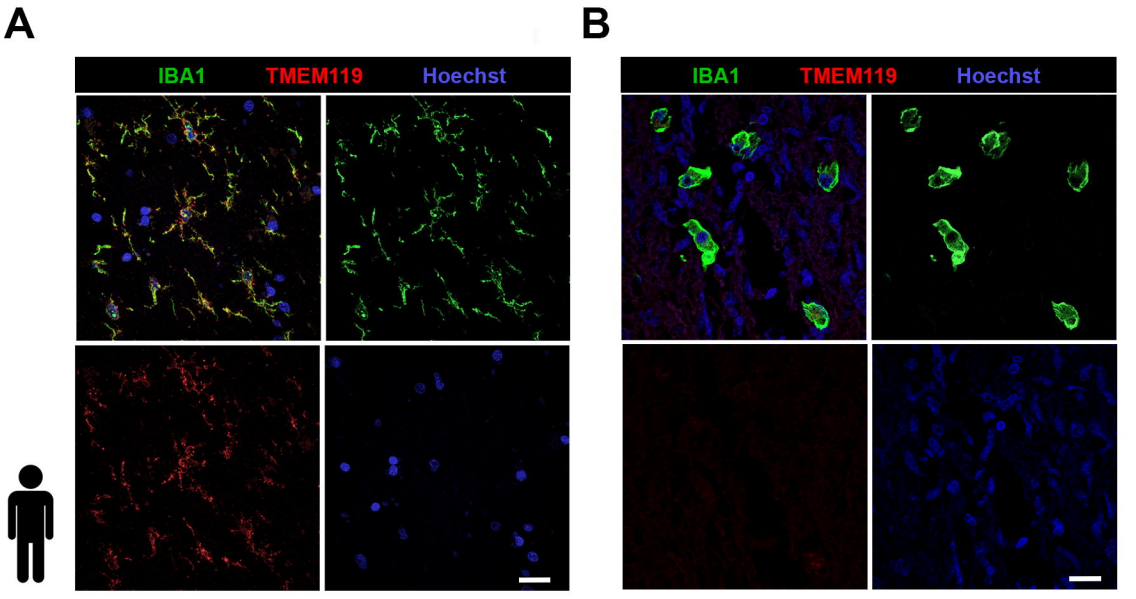

Suppl. figure 11

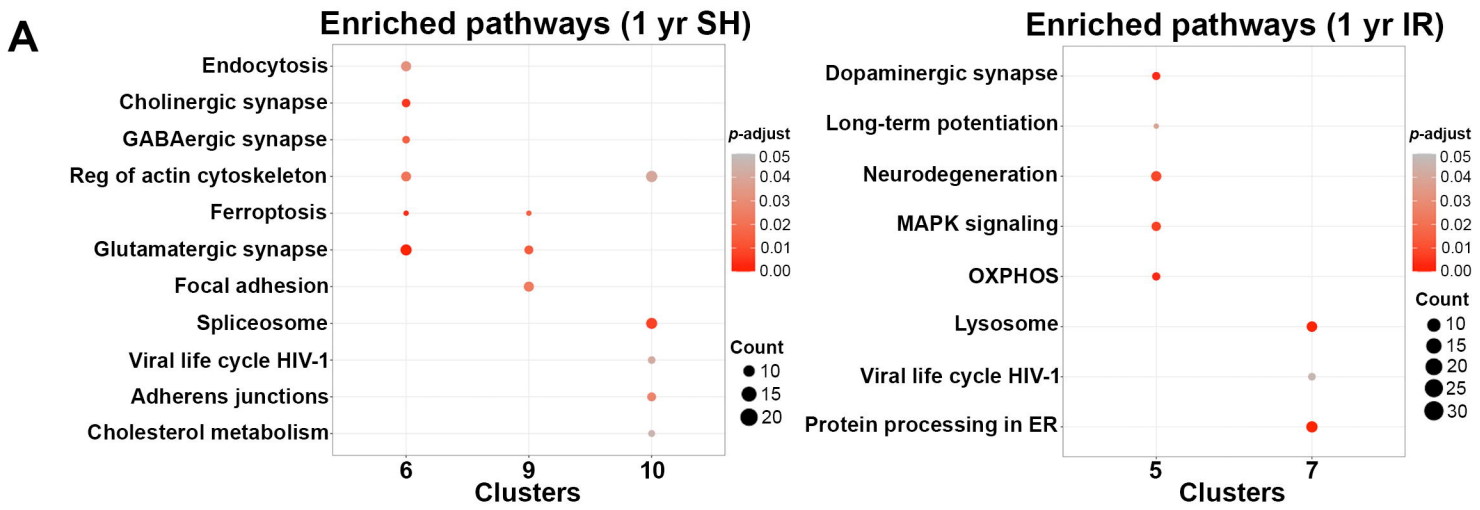

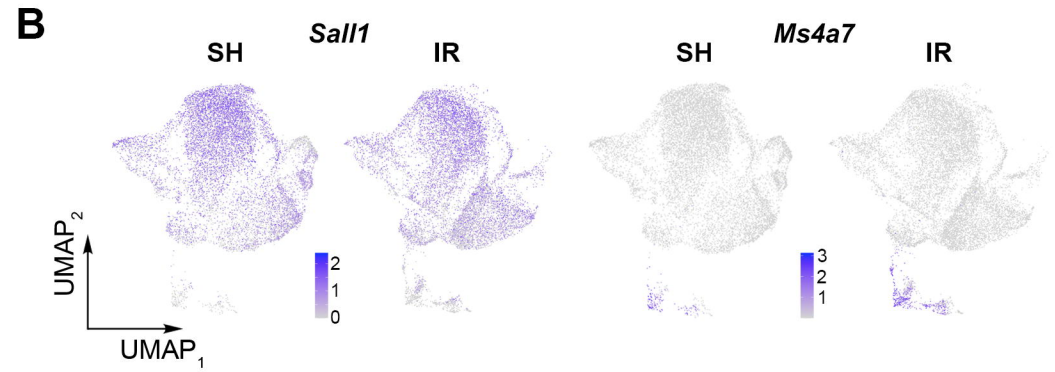

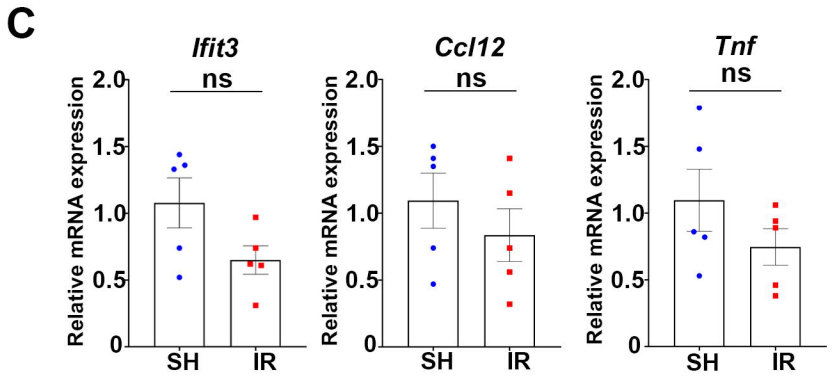

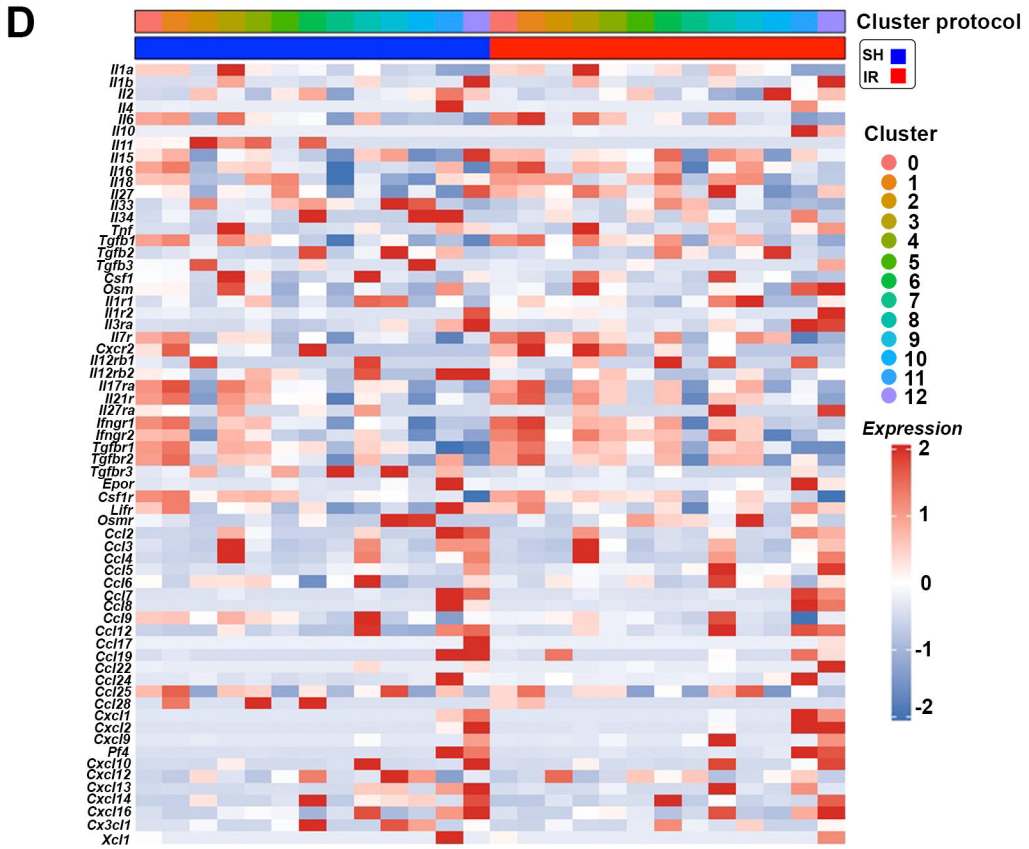

Suppl. figure 12

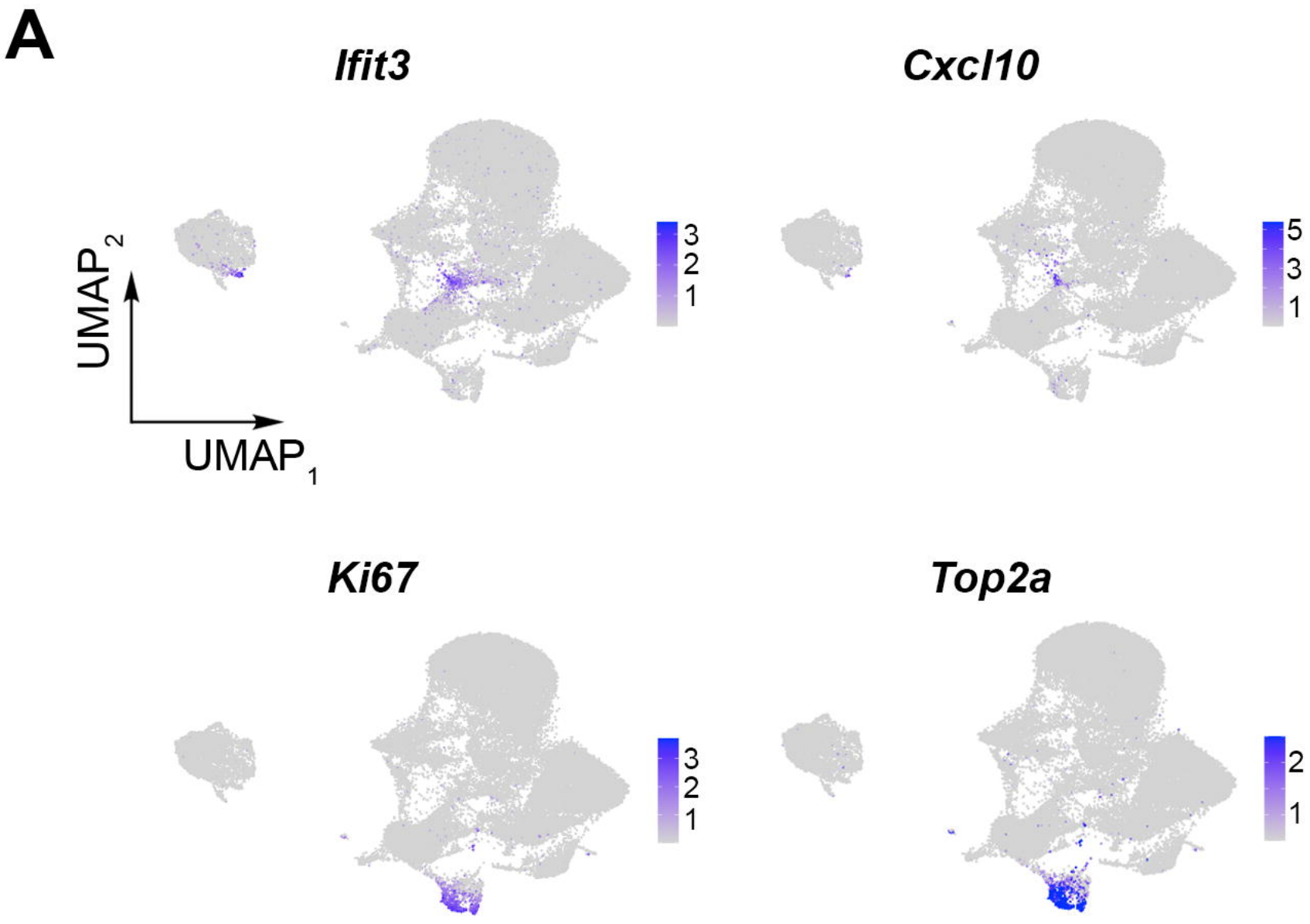

Suppl. figure 13